

Mémoire

Auteur : Faulx, Elise

Promoteur(s) : Nicolay, Samuel; Fettweis, Xavier

Faculté : Faculté des Sciences

Diplôme : Master en sciences géographiques, orientation global change, à finalité approfondie

Année académique : 2023-2024

URI/URL : <http://hdl.handle.net/2268.2/21056>

Avertissement à l'attention des usagers :

Tous les documents placés en accès ouvert sur le site le site MatheO sont protégés par le droit d'auteur. Conformément aux principes énoncés par la "Budapest Open Access Initiative"(BOAI, 2002), l'utilisateur du site peut lire, télécharger, copier, transmettre, imprimer, chercher ou faire un lien vers le texte intégral de ces documents, les disséquer pour les indexer, s'en servir de données pour un logiciel, ou s'en servir à toute autre fin légale (ou prévue par la réglementation relative au droit d'auteur). Toute utilisation du document à des fins commerciales est strictement interdite.

Par ailleurs, l'utilisateur s'engage à respecter les droits moraux de l'auteur, principalement le droit à l'intégrité de l'oeuvre et le droit de paternité et ce dans toute utilisation que l'utilisateur entreprend. Ainsi, à titre d'exemple, lorsqu'il reproduira un document par extrait ou dans son intégralité, l'utilisateur citera de manière complète les sources telles que mentionnées ci-dessus. Toute utilisation non explicitement autorisée ci-avant (telle que par exemple, la modification du document ou son résumé) nécessite l'autorisation préalable et expresse des auteurs ou de leurs ayants droit.



Faculté des sciences
Département de géographie

Frequency analysis of temperature and ENSO data: modal extraction

MASTER THESIS PRESENTED BY: ELISE FAULX

MASTER IN GEOGRAPHY, GLOBAL CHANGE, CLIMATOLOGY

ACADEMIC YEAR : 2023-2024

PRESENTATION AND DEFENSE : SEPTEMBER 2024

JURY PRESIDENT : PR XAVIER FETTWEIS

PROMOTER : PR. SAMUEL NICOLAY

CO-PROMOTER : PR. XAVIER FETTWEIS

LECTURE JURY : PR. GEORGES MABILLE

DR. CHRISTOPHE KITTEL

Acknowledgments

I would like to express my gratitude to all those who have supported me throughout the completion of this master's thesis.

First, I want to sincerely thank my supervisor, Samuel Nicolay, for his unwavering patience and guidance. His clear explanations, particularly regarding the mathematical aspects of my research, were invaluable.

I am also very grateful to my co-supervisor, Xavier Fettweis, for his insightful advice and constructive feedback.

A special thank you goes to my thesis readers, Christoph Kittel and Georges Mabilie. I am especially thankful to Georges Mabilie for generously providing the data that formed the backbone of my analysis.

I would also like to extend my appreciation to Courtney Hough for meticulously proofreading my thesis and helping refine my English.

Lastly, I want to express my deepest thanks to my family, who have been my pillars of support throughout these five years of study.

Abstract

The ENSO (El Niño Southern Oscillation) phenomenon is a complex climate process governed by various cycles, that are yet only partially understood. To better understand these cycles and their impact on the global climate, we employed a modal extraction method based on Continuous Wavelet Transform (CWT).

Most particularly, we used the Wavelet-Induced Mode Extraction (WIME) algorithm, initially developed to decompose signals into cosinusoidal components varying in frequency, amplitude, and phase. In this thesis, the WIME algorithm was adapted to handle real-world signals by incorporating adjustable parameters to manage noise, peak concavity, and frequency variation range.

ENSO was analyzed using two indices: the Southern Oscillation Index (SOI) for the atmospheric component and the Oceanic Niño Index (ONI) for the oceanic component. The method was validated by reconstructing signals for temperatures, ONI, and SOI, with correlation coefficients of 0.86, 0.94, and 0.76, respectively, demonstrating the robustness of the approach. The identified periods are consistent with each other and with existing literature. Moreover, the indicators remain strong when considering El Niño and La Niña events exclusively.

Furthermore, short- and medium-term predictions (2-3 years) were made by truncating the time series and testing the method's ability to forecast subsequent data. This validation procedure shows a correlation of 0.92 with the ONI signal and satisfactory difference indicators.

Understanding ENSO is vital due to its significant impacts on global weather patterns, economies, and ecosystems. This study introduces a novel approach for analyzing and forecasting the ENSO phenomenon, offering potential improvements in prediction accuracy. Additionally, this method has potential applications to other climate phenomena, such as the Arctic Oscillation and the North Atlantic Oscillation, as well as non-climatic events like seismic activities.

Contents

1	Introduction	13
1.1	Generalities	13
1.2	Motivations	14
1.3	Approach	15
1.4	Structure	15
2	Second Part: Climatic Aspects	17
2.1	ENSO-neutral	18
2.2	El Niño canonical events	19
2.3	La Niña canonical events	20
2.4	Modoki events	21
3	Third part : Mathematical and Computational Aspects	25
3.1	General Theory	26
3.1.1	Fourier transform	26
3.1.2	Convolution	27
3.1.3	Wavelets	28
3.2	Preprocess	30
3.2.1	Interpolation and average	30
3.2.2	Borders effects	30
3.3	The WIME algorithm	31
3.3.1	The wavelet used in WIME	31
3.3.2	Algorithm description	32
3.3.3	Arguments	37
4	Fourth part : Temperature analysis	39
4.1	The Bierset temperature data (1956-2023)	40
4.2	Periods larger than 3 months	40
4.2.1	Arguments chosen	40
4.2.2	Reconstruction and validation	41
4.2.3	Periods	41
4.3	Daily periods	44
5	Fifth part: ENSO signal analysis	47
5.1	Different time series (1951-2023)	48
5.2	Arguments chosen	51
5.3	Reconstruction and validation	52

5.3.1	General validation	52
5.3.2	Extreme events validation	54
5.4	Periods	57
5.4.1	Low-frequency period	58
5.4.2	Mid-frequency periods	60
5.4.3	High frequency periods	61
6	Sixth part: Predictions	65
6.1	Method	66
6.1.1	Amplitude extrapolation	66
6.1.2	Argument extrapolation	67
6.2	Validation	68
6.3	Future predictions	73
7	Seventh part: Discussion	75
7.1	Correspondence between expected and obtained results	76
7.1.1	Cycles in Temperature	76
7.1.2	Cycles in ENSO indices	76
7.1.3	Potential impact of Global Change	77
7.2	Limitations and perspectives	79
7.2.1	A usefulness for predictions	79
7.2.2	Periods and phase extrapolations	80
7.2.3	ENSO indices chosen	82
7.2.4	Perspectives for other phenomena	83
8	Conclusions	85

List of Abbreviations

AO	Arctic Oscillation
CWT	Continuous Wavelet Transform
DWT	Discrete Wavelet Transform
ENSO	El Niño Southern Oscillation
IP	Inflection Point
m.	months
NAO	North Atlantic Oscillation
ONI	Oceanic Niño Index
QBO	Quasi-Biennial Oscillation
RMSE	Root Mean Square Error
SLP	Sea Level Pressure
SOI	Southern Oscillation Index

SST **Sea Surface Temperature**

Std **Standard deviation**

WIME **Wavelet-Induced Mode Extraction**

WWB **Westerly Wind Bursts**

List of symbols

\overline{x}	Average
$ x $	Absolute value
\mathbb{R}	Set of real numbers
L^p	The Lebesgue space
\hat{f}	Fourier transform of a function f
t	Time
y	Frequency
f	Time serie function
P	Polynomial
ω	Window function
x	Window position
ξ	Size parameter of the window

ξ^* ξ maximum (or most relevant), i.e. period

ψ Wavelet

W_f CWT of f

c A cosine component of f

A_i^* Amplitude of c_i

$argW_i^*$ Argument of c_i

ϕ_i^* Phase of c_i

1 Introduction

1.1 Generalities

The climate system is complex and encompasses many intrinsically linked processes. The El Niño-Southern Oscillation (ENSO) is the primary source of interannual variability in the Earth’s climate. This climatic phenomenon involves both oceanic and atmospheric components occurring in the equatorial Pacific. It is more widely known by its positive and negative phases, respectively El Niño and La Niña events, which occur between ENSO-neutral phases (Huang **and others** 2024; Saint-Lu **and** Leloup 2016).

ENSO is non-linear and characterised by different cycles, that may vary over time. Therefore, it remains a complex phenomenon, with cycles that are still poorly understood despite decades of research (Saint-Lu **and** Leloup 2016; D. Dommenget **and others** 2013).

Since 1900, anthropogenic activities have led to a phenomenon now at the heart of many concerns, namely climate change. The main causes of the change are the emissions of various greenhouse gases. In addition to rising temperatures, it is marked by various consequences such as changes in precipitation patterns, ocean acidification, rising sea levels, more frequent and intense extreme weather events, and the disappearance of animal and plant species. Thus, climate change profoundly disrupts natural and, consequently, human systems (IPPC 2023; Z. Chen **and others** 2024).

This evolving global context significantly influences existing climatic phenomena, including ENSO. In this context, understanding these phenomena becomes crucial. Studies have shown that climate change promotes El Niño and La Niña events by increasing their frequency, lifespan, and intensity. Furthermore, atmospheric teleconnections will also undergo changes caused by climate change, such as the temperatures in the Indian Ocean. This context of climate change adds an additional layer of complexity to an already challenging phenomenon to comprehend (Z. Chen **and others** 2024).

1.2 Motivations

The two extreme phases of ENSO (El Niño and La Niña), can cause numerous disruptions, primarily in Asia and South America. A considerable amount of scientific literature has focused on studying their consequences.

Firstly, El Niño events alter weather conditions that lead to extreme events. These include extreme heat (Eggeling **and others** 2024), exacerbating the urban heat island effect (Nájera González **and others** 2024), wildfires (Cordero **and others** 2024), droughts in Afghanistan (Shukla **and others** 2024), China (Yin **and others** 2023), and India (Deivanayagam **and others** 2024), floods due to increased intense rainfall (Pelckmans **and others** 2024; Avalon-Cullen **and others** 2024; Nurdianti **and others** 2024) and temporary sea level rise (Pelckmans **and others** 2024; Arcodia **and others** 2024), tropical cyclones in the Atlantic Ocean (Mueller **and others** 2024), in China (Zheng **and others** 2024), or landslides in the Andes (Vega **and others** 2024).

Secondly, these climatic consequences impact terrestrial and marine ecosystems. For example, recent studies have shown that they influence the water resources necessary for Chilean terrestrial ecosystems (Espinoza **and others** 2024) and those of the Amazon rainforest (Rodrigues **and others** 2024), that variations in oxygen levels affect marine ecosystems (Deng **and others** 2024), and that sea surface temperature anomalies cause coral bleaching in the Great Barrier Reef (Gregory **and others** 2024).

Finally, some authors have investigated the impacts that El Niño and La Niña can have on human populations. ENSO events can cause economic consequences (Smith **and** Ubilava 2017), affect agriculture (Shukla **and others** 2024), and even contribute to civil conflicts (Hsiang **and others** 2011). Additionally, health impacts have been studied, showing that La Niña events increase the amount of ozone, CO, and water vapor in the troposphere in Asia, particularly in China (Alladi **and others** 2024; X. Wang **and others** 2024).

However, ENSO is a local phenomenon with global impacts, which are not limited to Asia and Latin America. Researchers have highlighted similar problems caused by El Niño and La Niña events in South Africa (Shikwambana **and others** 2022), Antarctica (J. Wang **and others** 2023), and even Europe (Beverley **and others** 2024).

The objectives of this thesis are twofold: it aims both to understand the climate cycles influenced by ENSO (in the context of climate change) and to predict the

future value of ENSO indices. Indeed, predicting climatic phenomena, although ambitious, is crucial for anticipating and thus minimizing the climatic and societal risks associated with El Niño and La Niña episodes.

1.3 Approach

This Master thesis relies on a mathematical method particularly suited for analyzing climatic signals: Continuous Wavelet Transform (CWT). Wavelets allow for the decomposition of complex signals and help identify features that are sometimes invisible in Fourier Transform analysis. It is a powerful tool that has already yielded intriguing results in climatology (Mabille **and others** 2012; Samuel Nicolay 2006; Delière **and** S. Nicolay 2017).

This Master thesis builds upon the PhD research of Pr. Georges Mabilie, who applied the wavelet transform to various climatic signals, including temperatures, to identify previously unknown cycles. The main difference is that the method used by Mabilie did not provide components that evolved in frequency and phase (amplitude evolution was present but its evolution analysis was not published). This improvement is particularly significant in the study of ENSO, as the characteristics of this phenomenon evolve over time (Mabille 2014).

1.4 Structure

This thesis is structured in four key stages. The first part addresses the theoretical aspects (Sections 2 and 3). It includes:

- A review that explains the different phases of the ENSO phenomenon and the processes involved in their development.
- An overview of the mathematical foundations, starting with Fourier Transform to build the necessary understanding for Continuous Wavelet Transform.
- A comprehensive description of the new version of the WIME algorithm and its implementation.

The second part involves a brief test of the proposed algorithm on temperature data to demonstrate its performance (Section 4). A brief connection will be made with the analysis conducted by Mabilie during his PhD.

Thirdly, this method will be applied to the ENSO phenomenon. Most particularly,

We will consider two indices widely used: ONI and SOI (Sections 5 and 6). Three types of results will be presented:

- A reconstruction of these indices from 1951 to 2023.
- A description of the various cycles, focusing on the changes in their importance (amplitude) and frequency.
- A future prediction up to 2027.

Finally, we will discuss the limitations and perspectives of the results obtained and their comparison to those reported in the literature cited (Section 7).

2 Second Part: Climatic Aspects

In this first theoretical section, each phase of the ENSO phenomenon is rigorously described, including the following situations: ENSO-neutral (non-extreme events), canonical El Niño (also called EP El Niño), canonical La Niña (also called EP La Niña), El Niño Modoki (also called CP El Niño), and La Niña Modoki (also called CP La Niña).

We will focus on the disturbance (or lack thereof) of the Walker cell, the mechanisms of initiation and persistence, the lifespan, and its (regional and global) consequences.

We will see that ENSO is a non-linear phenomenon, regarding the spatial pattern, its (regional and global) consequences, amplitude, and time evolution (D. Dommenget **and others** 2013).

2.1 ENSO-neutral

Under normal conditions, an atmospheric circulation cell develops along the equator, between Central America (longitude 80°W) and Oceania (longitude 120°E): the Walker cell (green arrows in Figure 1). At the surface, the trade winds (eastward winds) blow towards the west. At these latitudes, the influence of the Coriolis force is almost negligible. Therefore, these winds follow the equator without deviating. This creates an anticyclone (dry weather) off the Latin American coast and a depression (humid weather) around Australia. Naturally, this pressure difference reverses at altitude, at the tropopause level (between 15 and 18 kilometers since we are at the equator), and creates a high-altitude atmospheric current in the opposite direction, from west to east (Ashok **and** Yamagata 2009; Saint-Lu **and** Leloup 2016). What

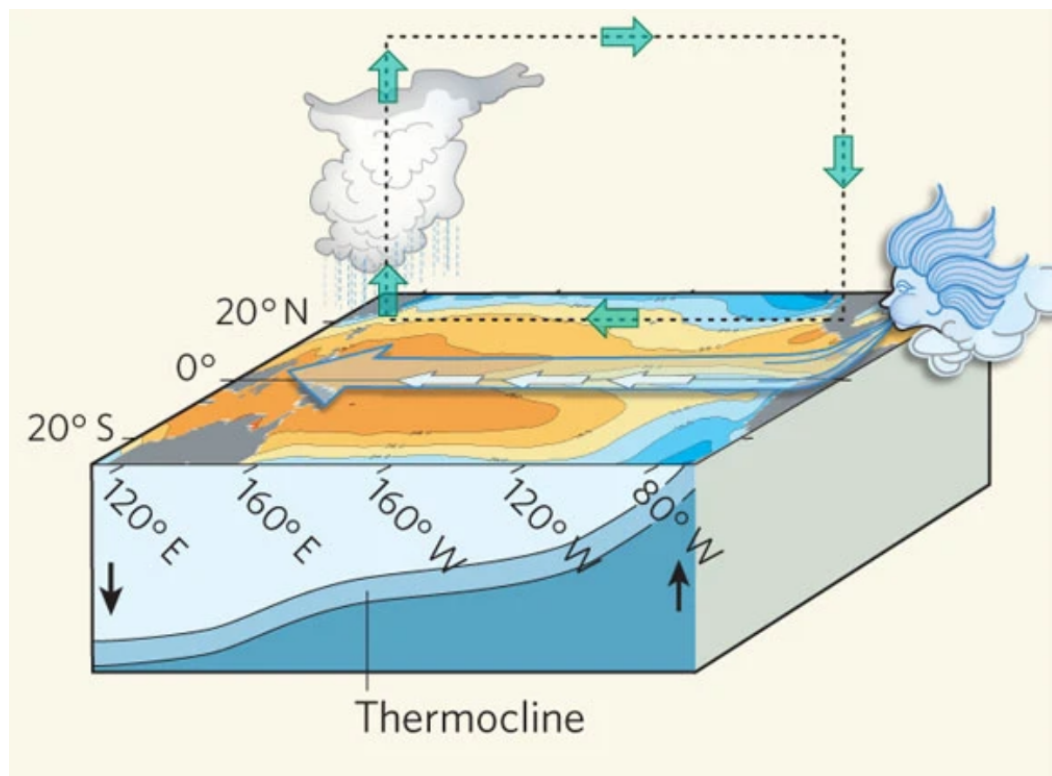


Figure 1: Schema of Walker Cell, a normal condition in the tropical Pacific (Ashok **and** Yamagata 2009).

Color code: water temperature (red for warm and blue for cold).

Green arrows: atmospheric circulation.

Blue arrows: oceanic circulation.

Black arrows: thermocline movement

characterizes the Walker cell is the relationship between atmospheric and oceanic currents. Indeed, the trade winds push the surface water, causing an oceanic current in the same direction, from east to west (blue arrows in Figure 1). On one hand,

this creates a pressure deficit close to the American continent, causing cooling in the area due to the upwelling of much colder deep water. This is also evident in Figure 1, with the thermocline approaching the surface, at the east of the cell. In the other hand, these trade winds maintain (and confine) the warm pool, a reservoir of warm waters with temperatures exceeding 28 °C, located around Papua New Guinea (dark orange in Figure 1). This warm pool, in turn, fuels atmospheric convection (Ashok **and** Yamagata 2009; Saint-Lu **and** Leloup 2016).

This initial case can be considered as an ENSO-neutral state. But, as we will see below, this balance is not immutable.

2.2 El Niño canonical events

When the direction of the circulation cell and the ocean current reverses, This situation is called "El Niño," or "El Niño canonical," and is shown in Figure 3a.

In this case, meteorological conditions also reverse: a depression over the American continent and an anticyclone over the Australian islands. The upwelling of cold water along the Latin American coasts stops and the warm pool extends through the east side, causing a clear increase in temperatures in the region. (Ashok **and** Yamagata 2009).

The different meteorological aspects of El Niño reinforce each other (positive feedback loop, i.e the Bjerkness feedback, see Figure 2). However, the initial triggers for an El Niño event are still a subject of controversy (Saint-Lu **and** Leloup 2016; Eusebi Borzelli **and** Carniel 2023). It could be either:

- A. Initiation by atmospheric dynamics: weakening of trade winds and/or activation of WWB (westerly wind bursts). The latter would be a key triggering factor. Indeed, the correlation coefficient between the annual frequency of 150°E WWB and the year-end ENSO observation is 0.82 (Eusebi Borzelli **and** Carniel 2023; M. Wang **and others** 2023).
- B. Initiation by oceanic dynamics: Less water is brought up to the surface (reduction or cessation of upwelling), and the upwelled water is warmer (lowering of the thermocline) along the Latin American coast (Eusebi Borzelli **and** Carniel 2023).
- C. Initiation by changes in oceanic temperature: expansion of the Warm Pool and/or increase of SST in the East (Eusebi Borzelli **and** Carniel 2023).

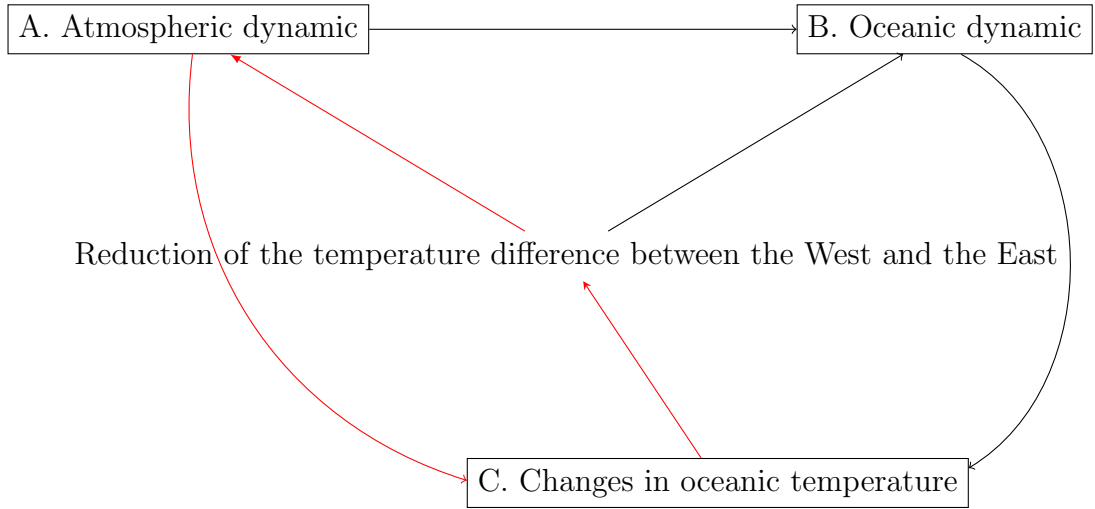


Figure 2: Positive feedback loops in El Niño Event. Red arrows represent the Bjerkness feedback

El Niño episodes almost always occur in the summer of the Southern Hemisphere, typically peaking in December, after which their intensity rapidly decreases. Most of the time, their total duration is less than 12 months (M. Chen **and** T. Li 2018).

These abnormal conditions can have a variety of consequences, ranging from floods and a decrease in fishery resources (related to the absence of upwelling) in Latin America to droughts, fires, and an increase in epidemics for Australia and its islands. However, the consequences are not limited to the tropical Pacific Ocean but extend globally. During El Niño years, the global temperature increases. That is why the El Niño phase is referred to as the **"warm phase"** of the ENSO phenomenon (Gurdjian 2023; Ashok **and** Yamagata 2009).

2.3 La Niña canonical events

La Niña situations correspond to a strengthening of normal conditions: the trade winds blow stronger, the warm pool is reduced (more confined to the Oceania region), upwelling is more pronounced, and the thermocline is even closer to the surface as one moves towards Latin America. This can be seen in Figure 3c. Naturally, the meteorological conditions in Oceania and Latin America are similar to those described in the Section 2.1, dedicated to ENSO-neutral (Ashok **and** Yamagata 2009).

Generally, a La Niña episode is triggered shortly after an El Niño episode has completely finished. These are negative feedback loops, mainly associated with

thermocline depth, that lead to a transition from El Niño to La Niña. However, unlike El Niño, once La Niña conditions are established, the phenomenon lasts much longer. Indeed, once its peak is reached, the intensity decreases slowly over the first 6 months and then evolves either into an ENSO-neutral situation or into another La Niña episode. This latter situation corresponds to a phenomenon called "multiyear La Niña" (M. Chen **and** T. Li 2018; Saint-Lu **and** Leloup 2016; D. Dommenget **and others** 2013).

Similar to El Niño, La Niña has meteorological consequences on a global scale, but they are considered less severe than those of El Niño. They correspond neither to the "opposite of El Niño consequences" nor to the "amplification of the ENSO-neutral condition". La Niña is referred to as the "**cold phase**" of the ENSO phenomenon, as the Global temperature is lower during this phase (Saint-Lu **and** Leloup 2016).

2.4 Modoki events

The major difference between canonical events and Modoki events lies in the fact that the temperature anomaly is located in the central Pacific. That's why they are also called CP (Central Pacific) El Niño or CP La Niña, in contrast to canonical events, which are also called EP (Eastern Pacific) El Niño or EP La Niña. Moreover, Modoki events would have a more meridional extension than canonical events (D. Dommenget **and others** 2013; Pal **and others** 2020).

They are controlled by different dynamics than canonical events. The causes that would trigger the onset of these events are multiple, varied, and not yet well understood. Even though more and more studies are made to understand their functioning, Modoki events are much less well-known than canonical episodes. They are also less easy to detect. Indeed, the most commonly-used current indicators generally lead either to an omission of these events or to an impossibility of determining whether it is canonical or Modoki (D. Dommenget **and others** 2013; Kulkarni **and** Siingh 2016).

They also have global-scale consequences, but they differ from the consequences of canonical events and are still uncertain. (Dogar **and others** 2019).

On one hand, El Niño Modoki corresponds to a warm anomaly in the central Pacific (associated with a depression), surrounded by cold anomalies to the west and east (associated with anticyclones). These conditions are represented in Figure

3b. Almost always, an El Niño Modoki episode is less powerful than a canonical El Niño episode but they would be as powerful as canonical La Niña events.

The first theory to explain the onset of El Niño modoki condition is, unlike canonical El Niño events, El Niño Modoki may not be triggered by WWBs (or the WWBs would blow much less strongly), which would not induce the thermocline response to the east. Some hypotheses highlight the importance of SST anomalies or propose a subtropical and extra-tropical origin linked to SLP variability (D. Dommenget **and others** 2013; Pal **and others** 2020; He **and others** 2021; Jin-Yi Yu **and** Lee 2010; J.-Y. Yu **and** Kim 2011; Jadhav **and others** 2015).

On the other hand, La Niña Modoki corresponds to a cold anomaly in the central Pacific (anticyclone) surrounded by warm anomalies (where depressions form). These specific conditions are schematically represented in Figure 3d. They would be slightly more powerful than canonical La Niña events. This type of event would occur after a canonical El Niño if the extratropical and subtropical SLP conditions are "favorable" (D. Dommenget **and others** 2013; Pal **and others** 2020; J.-Y. Yu **and** Kim 2011).

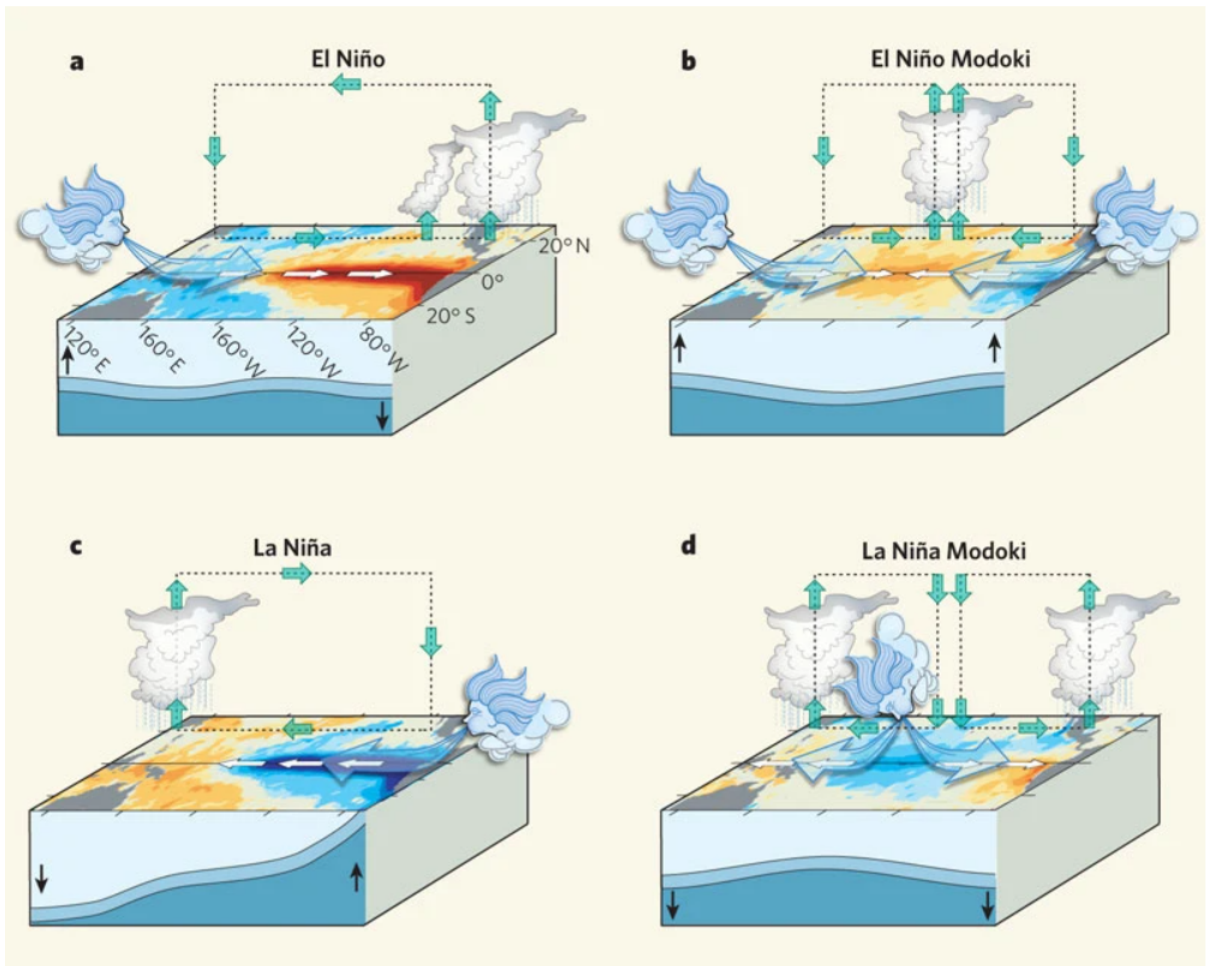


Figure 3: Schema of different ENSO conditions.

a. El Niño canonical; b. El Niño modoki; c. La Niña canonical; d. La Niña modoki.

Color code: water temperature (red for warm and blue for cold).

Green arrows: atmospheric circulation.

Blue arrows: oceanic circulation (Ashok **and** Yamagata 2009).

Black arrows: thermocline movement.

3 Third part : Mathematical and Computational Aspects

This theoretical part provides the foundations necessary for the understanding of two fundamental mathematical concepts within this thesis: the CWT and wavelets.

For their comprehension, it is inevitably necessary to address the Fourier transform and the convolution product.

Following this, we will describe the methodology through computational aspects, considering preprocessing, the principles of the algorithm itself and its arguments.

3.1 General Theory

3.1.1 Fourier transform

Definition 1 (The Lebesgue space L^p). The space L^p , with $1 \leq p < \infty$, refers to the **vector space** of functions defined on \mathbb{R} , measurable, and for which the p -th power of the absolute value is integrable. Thus, we have:

$$\sqrt[p]{\int |f|^p dt} < \infty \quad (1)$$

Hence, the space L^1 simply refers to a space of functions which are integrable.

Definition 2 (Fourier transform). If $f \in L^1$, the function $t \mapsto e^{\pm ity} f(t)$ also belong to L^1 . The positive Fourier transform of f with respect to y is denoted \hat{f} and is defined as:

$$\hat{f}(y) = \int_{-\infty}^{\infty} f(t) e^{ity} dt \quad (2)$$

The negative form is denoted \check{f} and is defined as:

$$\check{f}(y) = \int_{-\infty}^{\infty} f(t) e^{-ity} dt \quad (3)$$

This is a parametric integral with parameter y and integration variable t . The letter t is chosen to signify that the integral is performed over a time series. The parameter y plays the role of frequency or angular frequency, and the Fourier transform \check{f} corresponds to some average of all frequencies.

A function and its Fourier transform are two different views of the same function: the function f corresponds to its temporal view and its Fourier transform \check{f} corresponds to its frequency view. There is a unique correspondence between these two points of view. Therefore, if it is possible to compute the Fourier transform from the function (Equation 2 and 3), it is likewise possible to recover the function from its transform. The Fourier theorem establishes a connection between a Fourier transform and its corresponding function.

Theorem 3 (Fourier theorem). If $f \in L^2$ then its Fourier transform also belongs to L^2 ; in fact, the Fourier transform is a linear isometry from L^2 to L^2 and we have

$$\check{\check{f}} = \hat{\hat{f}} = 2\pi f \quad (4)$$

This can be accomplished using the IFFT (Inverse Fast Fourier Transform)

function in Scilab (Oppenheim **and** Schafer 1975).

3.1.2 Convolution

Definition 4 (Convolution product). Let f and ω be two functions defined on \mathbb{R} . If $x \in \mathbb{R}$ and the function $t \mapsto f(t) \omega(x - t) \in L^1$ for all x , then its integral, called 'convolution product', is denoted as $(f * \omega)$ and is given by:

$$(f * \omega)(x) = \int_{-\infty}^{\infty} f(t) \omega(x - t) dt \quad (5)$$

Due to the vector space nature of L^1 (see Definition 1), these conditions are fulfilled as soon as $f \in L^1$ and $\omega \in L^1$.

In the context of this thesis, the function f will represent the time series (temperature, ENSO index, etc.), and the function ω will correspond to the "window" function. Schematically, x represents the position of the window ω center along the time series and $(f * g)(x)$ represents the data around x smoothed by the window ω .

The window function ω_ξ can be defined mathematically by $t \mapsto \omega\left(\frac{t}{\xi}\right)$. The definition of the factor ξ varies depending on the context, but it is always related to the intrinsic size of the window ω_ξ . Consider the temporal view: if the window has a compact support (for example, as moving averages), the factor ξ simply corresponds to the size of the function. However, in most cases, the support is not compact and another method is needed to account for the size. For instance, the factor ξ for Gaussian functions (and their derivatives), generally refers to the standard deviation (or inflection point) of the curve.

The windows ω should be a differentiable function, ensuring that the convolution $(f * \omega)$ is also differentiable.

Property 5. The derivative of the convolution $f * \omega$ with respect to y is given by:

$$\frac{d}{dx}(f * \omega)(x) = (f * \frac{d}{dx}\omega)(x) \quad (6)$$

Property 6. The Fourier transform of the convolution product is given by:

$$\widehat{(f * \omega)} = \hat{f} \hat{\omega} \quad (7)$$

Thus, executing the Fourier transform of the convolution $(f * \omega)$ is roughly

equivalent to multiplying the frequencies of the time series \hat{f} with the frequencies of the window $\hat{\omega}$.

3.1.3 Wavelets

Definition 7 (wavelet). A wavelet, denoted as ψ , is a function that belongs to $L^1 \cap L^2$ and satisfies the following admissibility condition:

$$\int_{-\infty}^{\infty} \frac{|\psi(\hat{y})|^2}{|y|} dy < \infty \quad (8)$$

Property 8 (Admissibility condition). If the admissibility condition is satisfied, the integral of ψ is zero. Note that this is equivalent to saying that the Fourier transform of ψ at 0 is zero.

$$\int_{-\infty}^{\infty} \psi(t) dt = \int_{-\infty}^{\infty} \psi(t) e^0 dt = \int_{-\infty}^{\infty} \psi(t) e^{\pm it0} dt = \hat{\psi}(0) = 0 \quad (9)$$

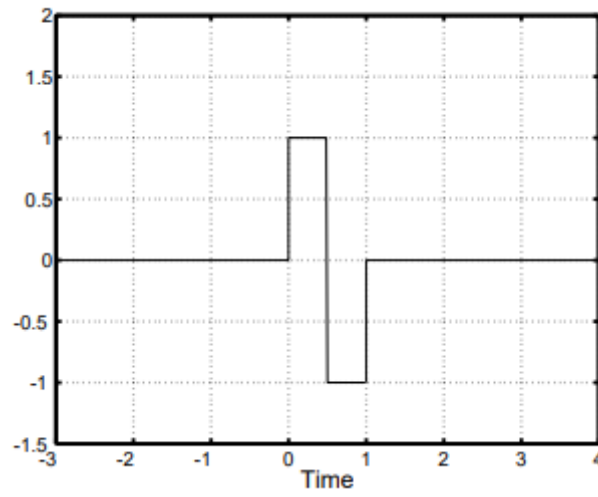
For example, we have the "poor man's wavelet" (Figure 4a), the "Mexican hat wavelet" (Figure 4b), or the Morlet wavelet (Figure 4c). We can easily check that their integrals are equal to zero. Note that for Morlet wavelet, the condition setted by the Equation 9 is nearly respected because its fourier transform at 0 is "almost equal to 0" ($\hat{\psi}(0) = 4 \cdot 10^{-6}$).

Definition 9 (Continuous wavelet transform). The CWT (Continuous Wavelet Transform) entails the convolution of f , defined on L^2 , with the wavelet ψ_ξ for all positive values of the size parameter ξ , and position x . It is given by:

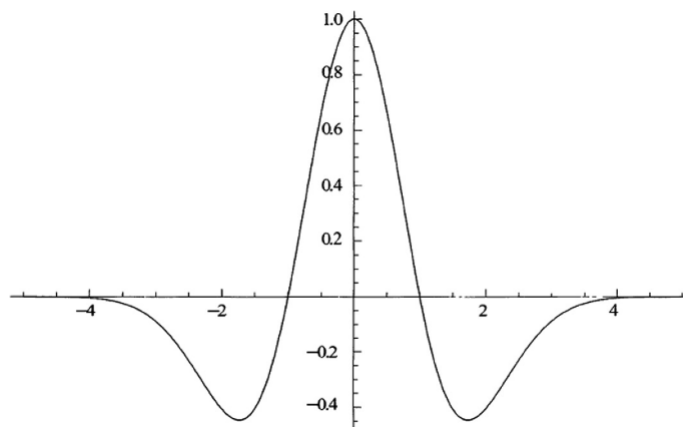
$$W_f(x, \xi) = \int f(t) \psi\left(\frac{x-t}{\xi}\right) \frac{dt}{\xi} = \frac{1}{\xi} (f * \psi_\xi(x)) \quad (10)$$

In other words, the wavelet ψ assumes the role of ω in Section 3.1.2. We can observe that the factor $\frac{1}{\xi}$ in (10), where ξ corresponds to the size parameter of the wavelet, acts as a renormalization factor, preserving some norm.

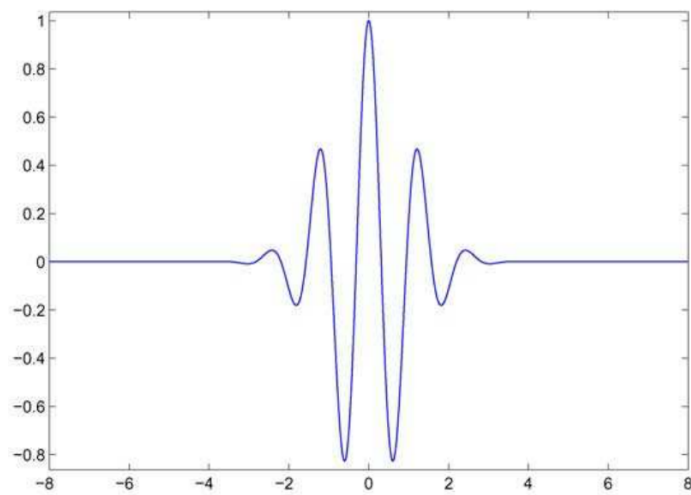
In the context of time-frequency analysis, we will perform the convolution product between a wavelet ψ and a time series f , over all possible window sizes ξ , and across the entire time series. Low values of ξ will be suited for low frequencies, while high values of ξ will be suited for high frequencies.



(a) Poor man's wavelet



(b) Mexican hat wavelet



(c) Morlet wavelet

Figure 4: Exemple of famous wavelets

Definition 10 (wavelet with m vanishing moments). A wavelet ψ has m vanishing moments ($m > 0$) if

$$\int_{-\infty}^{\infty} t^k \psi(t) dt = 0 \quad (11)$$

For every $k \in \mathbb{N}$ such that $k < m$,

Therefore, by definition (see Definition 7), a wavelet always has at least one vanishing moment. The value of m corresponds to the maximum degree of the trend polynomial for which the wavelet is blind. More precisely, if ψ has m vanishing moments and if P is a polynomial of degree at most $m - 1$, we have:

$$W_P(x, \xi) = \int P(t) \psi\left(\frac{x-t}{\xi}\right) \frac{dt}{\xi} = 0 \quad (12)$$

As we are primarily interested in periods, disregarding trends, the robustness of a wavelet increases as its number of zero moments grows.

3.2 Preprocess

3.2.1 Interpolation and average

WIME requires the input signal with a constant time step. Thus, this step is crucial to enable the use of signals with varying time steps. The temporal resolution can then be upgraded (linear interpolation) or downgraded (averaging). As will be discussed in Section 4.3, this is the case for the Bierset temperature data.

3.2.2 Borders effects

Borders effects occur when a portion of the window (wavelet ψ_ξ) evaluates undefined values of the time series f . As the size of the window ξ (or the target period) increases, the quantity of data affected by the issue of edge effects grows.

Mathematically speaking, let us consider f , defined by a set of values y_t with t defined in the interval $A =]0, n]$, where n is the total number of values present in the time series ($A \subset \mathbb{N}_0$). At time step t , ψ is defined over the set $B = \{y_{t-\frac{\xi}{2}}, \dots, y_{t+\frac{\xi}{2}}\}$, with ξ , the window size where $\frac{\xi}{2} \in \mathbb{N}_0$ ($B \subset \mathbb{N}_0$).

The time series f will experience edge effects when $t - \frac{\xi}{2} < 0$ and when $t + \frac{\xi}{2} > n$.

Consequently, the maximum size ξ of the window for which the series f is not affected by edge effects decreases as we approach the beginning or the end of the

time series.

To address this issue, we extrapolate both ends of the time series. Therefore, the size of the signal is artificially increased for analysis. The **"mirror" method**, widely used in climatology, was chosen for this thesis. Therefore, a "mirror" function was implemented in Scilab to preprocess the signals before they undergo the WIME algorithm.

$\forall t \in L =]-n, 0]$, we have

$$f(t) = f(-t) \quad (13)$$

$\forall t \in R =]n, 2n]$, we have

$$f(t) = f(2n - t) \quad (14)$$

With this method, the frequency information and signal continuity are preserved. In contrast to the **periodic method**, that causes jumps at the edges (the continuity is not preserved).

An example of a cosine function (given by the formula $y(t) = \cos(\frac{2\pi}{5} \cdot t)$, where t is arbitrarily defined in the interval $[-1.6, 15.6]$, is illustrated in Figure 5. The red dashed vertical lines separate the initial function from its mirror on the left (on the interval L) and on the right (on the interval R). They are located at 0 and n .

Furthermore, applying this method triples the size of the input signal, enabling the detection of larger periods.

3.3 The WIME algorithm

The algorithm WIME, standing for Wavelet-Induced Mode Extraction, is designed to extract the oscillatory components of a signal by performing CWT. A first version was outlined in Delière and Nicolay (2017) has since been adapted for this master's thesis.

3.3.1 The wavelet used in WIME

The "frequency view" of the wavelet used in WIME is represented by Figure 6a and given by the mathematical formula below:

$$\hat{\psi}(y) = \sin\left(\frac{\pi y}{2\Omega}\right) e^{-\frac{(y-\Omega)^2}{2}} \quad (15)$$

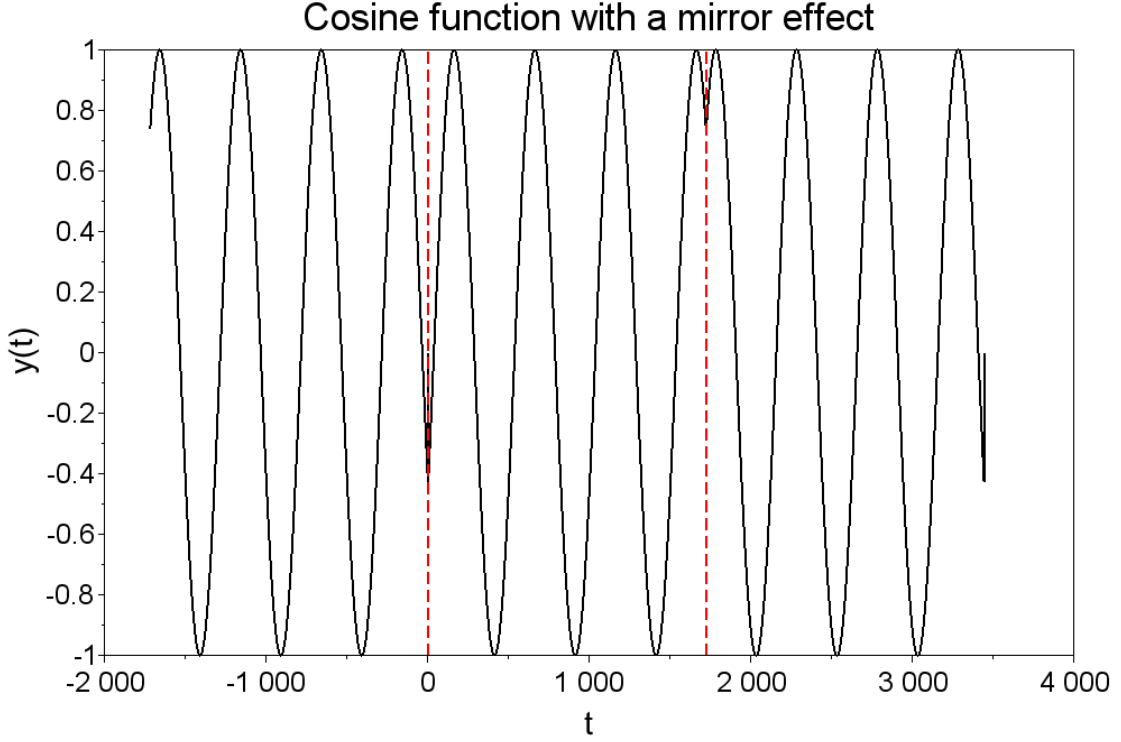


Figure 5: Example of the "Mirror method" applied to function $y(t) = \cos\left(\frac{2\pi}{5} \cdot t\right)$
Red dashed line in 0 and in n ($= 1720$)

With Ω , a parameter equal to $\pi\sqrt{\frac{2}{\ln 2}}$ or approximatively 5.336446.

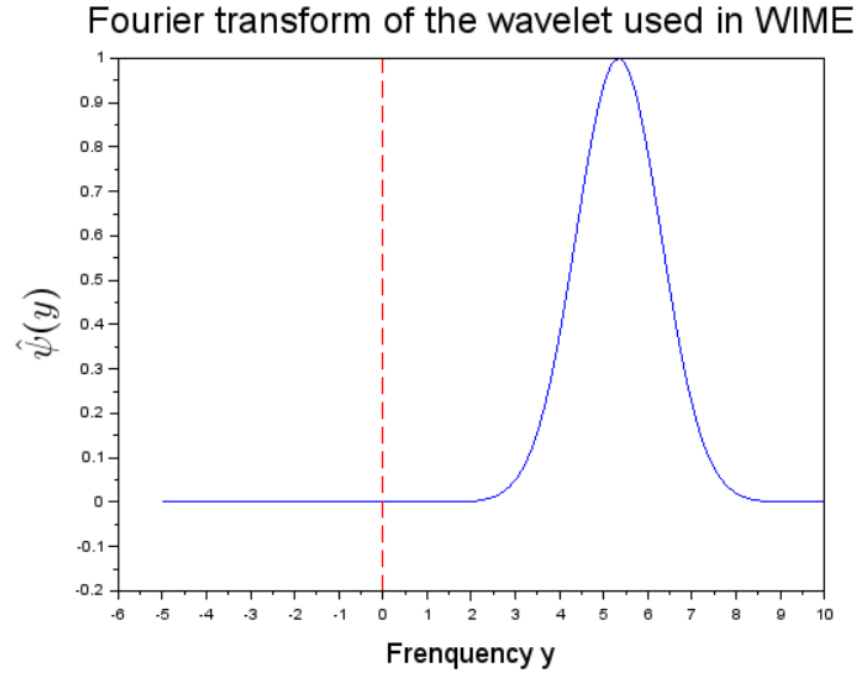
This wavelet is similar to the Morlet wavelet ψ_M , to which we have appended a sinusoidal factor. This addition enables the wavelet to adhere to property (8) : $\hat{\psi}(0) = \sin(0) \psi_M = 0$.

The "temporal view" can be obtained through the conversion of the frequency view using the Fourier theorem (see Equation 4), thanks to the Inverse Fast Fourier Transform (IFFT) function in Scilab. It is represented by Figure 6b, in which we can notice its Morlet-like aspect.

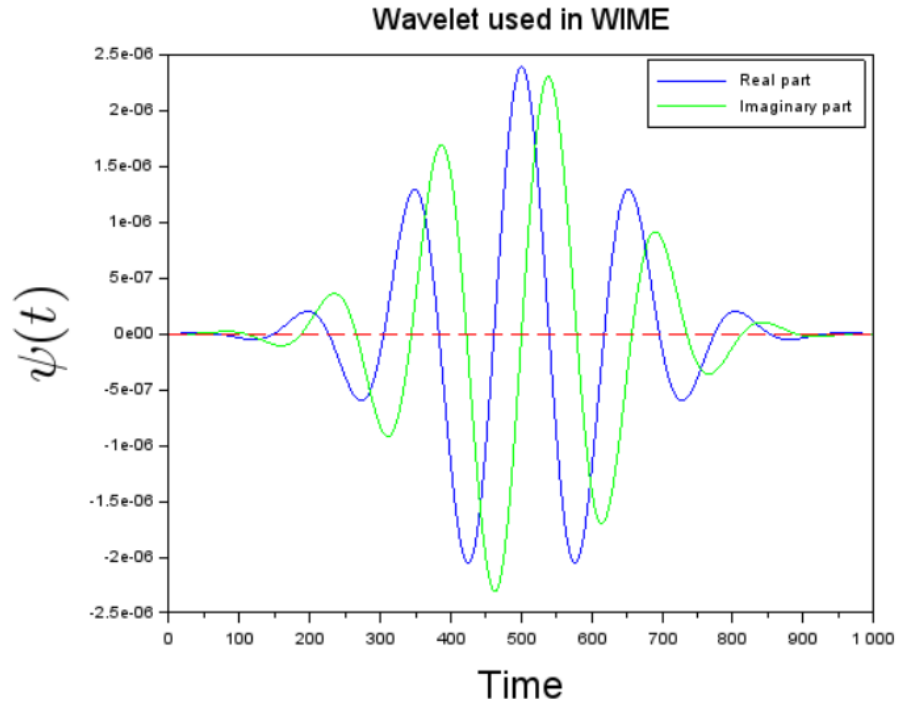
This wavelet is robust, with 4 numerically vanishing moments ($m=4$ in the context of Definition 10).

3.3.2 Algorithm description

Before initiating the component extraction process, the algorithm inspects the signal. It verifies that its dimension is correct, and returns an error message if



(a) Fourier transform (frequency view)
Red line in $\hat{\psi}(0)$



(b) Initial function (temporal view)

Figure 6: Wavelet used in WIME

it is not. To ensure that this new version of the algorithm takes into account the effects added to the borders, artificially increasing the size of the signal (see Section 3.2.2), we also record the actual position of the beginning and end of the time series. Finally, WIME removes the mean to obtain anomalies.

It then checks the other arguments introduced via the command line. It adds default parameters if they are not all included (or if the value -1 is introduced in their place) and returns an error message if there are too many arguments. Note that all arguments, whether present initially or added for this work, will be detailed in Section 3.3.3.

At each iteration i , the algorithm proceeds through a series of seven steps, described below. It successively identifies the different periods and their variations over time.

The **first step** consists of performing the CWT of f (see Definition 9). This is approximated by the function *wmd_cwt*, written in C and made available through the FFTW3 library (Frigo **and** Johnson 2005). It conducts a series of Discrete Wavelet Transforms (DWT), significantly enhancing computation speed. For each window size ξ , the result is a matrix A_i , containing an energy value for each time step and; and a matrix *argW_i*, containing the future arguments of the cosine function (see later in this subsection).

The **second step** involves a simple averaging $\bar{\xi}$ for each window size ξ over time, across the entire signal. This is thus an average of all columns of the matrix A_i . It is performed by the function *spectrum*, and the result is identically named.

After obtaining this spectrum, the algorithm searches for the most "relevant" maximum, which is considered as the "mean peak period", denoted as $\bar{\xi}_i^*$ within the mathematical framework. This is achieved by the functions *freqband* and *fpeaks*. This **third step** has undergone the most changes. Indeed, since this method had proven effective on theoretical signals, it seemed interesting to adapt it to empirical climate signals. Two modifications significantly improved them:

- **Integration of Concavity:** In the initial version of WIME, all peaks of the spectrum were detected but only the most energetic one was retained. In the context of this work, we also considered that the second derivative of the spectrum at peak locations should be less than a threshold, defined by the user's arguments (it must be "sufficiently negative"). If multiple peaks meet

this condition, the most energetic one will be retained. If none of the peaks meet this condition, the threshold is reduced by a factor of 2 until peaks meeting this condition are found.

- **Noise Neglect:** Periods shorter than a certain threshold, also defined by the user, are not considered.

Following the detection of the "mean peak period" $\overline{\xi_i^*}$, we analyse its temporal evolution in the **fourth step** (function *findridge*). In the previous version of WIME, the range within which the "peak period" ξ_i^* could vary upon its temporal position within the series. This presented an issue as it could lead to a gradual reduction in the period value, often converging into the noise zone with no escape. Such errors were pronounced, particularly when we surpassed the first (most energetic) periods. Consequently, a decision was made to impose fixed boundaries (adjustable by the user prior to programme execution) of the zone in which the maximum could be located. These bounds (lower bound and upper bound) depend on the position of the inflection point (IP) of the Gaussian-like curve (of the maximum ξ_i^* related to this iteration). IPs are detected by differentiation. Note that in this new version of WIME, it is impossible to have an upper bound higher than the maximum frequency, and it avoids some errors.

Subsequently, WIME initiates by selecting t_0 , the most energetic point within the zone between the two established bounds. This t_0 position serves as the starting point for WIME to progressively compute the period for each time step (forward and backward from t_0). At each time step, it will create a spectrum corresponding to the energy value at that time, considering only the premise zone. If there are no maxima, the period value remains unchanged. If there are multiple maxima, it will choose the most energetic one. The temporal evolution of the period is then extracted and referred to as the *ridge*.

The **fifth step** consists of extracting the sinusoidal component c_i associated with the ridge. It can be obtained using the formula:

$$c_i(t) = 2|A_i^*(t)| \cos[\arg W_i^*(t)] \quad (16)$$

The argument $\arg W_i^*$ of the cosine component embed both frequency and phase ¹. Amplitude A_i^* , frequency, and phase all vary over time.

¹ $\arg W_i^* = 2 \pi \frac{1}{\xi_i^*(t)} + \phi_i^*(t)$

An example of such a component is provided below (Figure 7). One can observe variations in frequency (period lengths) in amplitude (heights of extrema), and in phase.

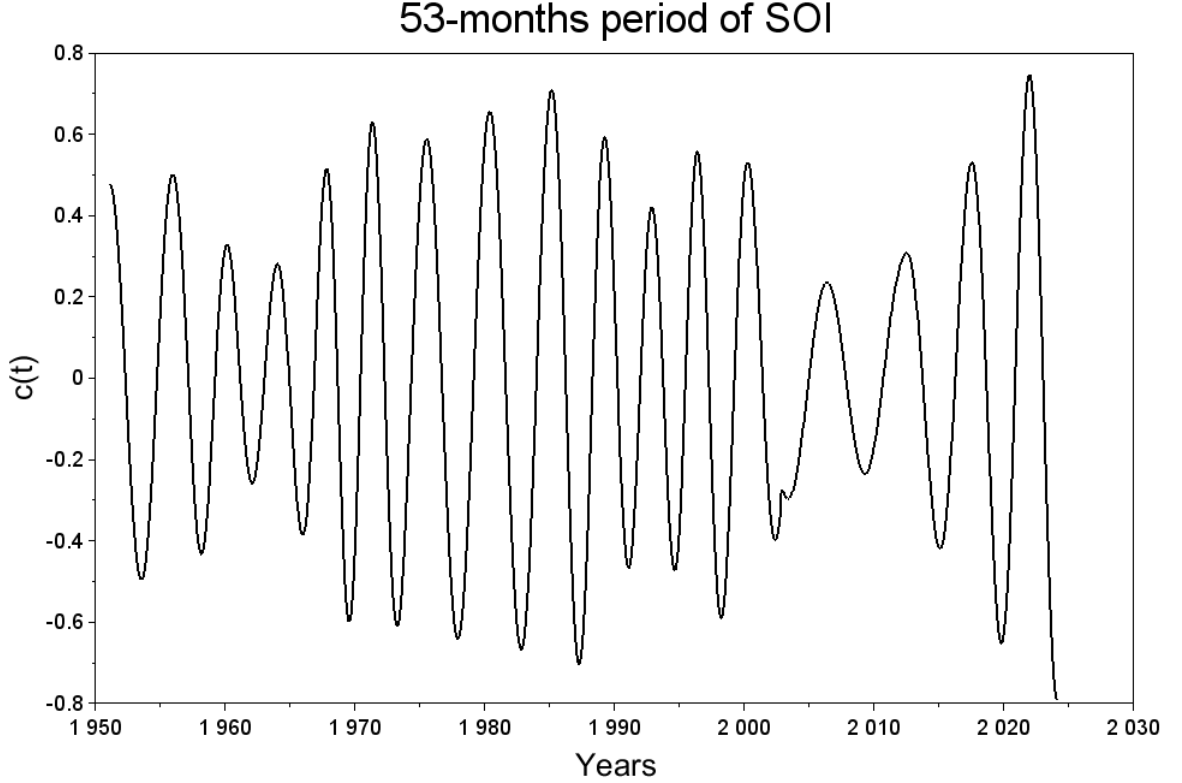


Figure 7: Example of a component extracted by WIME

The **sixth step** simply involves subtracting this component c_i from the signal to obtain the residue r_i :

$$\begin{aligned} \text{At the first iteration (i=1)} \quad & r_1 = f - c_1 \\ \text{At the second iteration (i=2)} \quad & r_2 = r_1 - c_2 \\ \text{At the third iteration (i=3)} \quad & r_3 = r_2 - c_3 \\ & \text{etc.} \end{aligned}$$

The seventh and **final step** generates graphs (if requested by the user through command line), and saves them in PNG format. It includes:

- **Matrix A_i :** Energy is depicted for each time step (rows) and for each window size ξ (columns). The higher the energy, the closer the color tends towards red. The ridge, and in the new version, the bounds, are also depicted on the matrix.

- **Spectrum $\bar{\xi}$:** The position of the chosen maximum $\bar{\xi}_i^*$ is also displayed on the spectrum.

Once these seven steps are completed, the algorithm saves, if requested by the user, the results of all iterations i as text files.

3.3.3 Arguments

For the purpose of this master thesis, we were interested in 4 parameters (in addition to the signal f) that were already present in the initial version of WIME. Firstly, there is a visualization argument (*visu*). When it is set to 1, the graphs are displayed (and now saved). The other arguments are stored in a vector called *wavpar*, which includes:

- *nOct*: the number of octaves. The default values (-1) correspond to the largest possible number of octaves. We set it at 40.
- *nVoice*: the number of voices between the octaves. We set it at 40 and -1 (the largest possible number of voices).
- *nIter*: the number of iterations i , and thus the number of detected periods.

For the purposes of this work, the following 7 parameters have been added.

- **Resolution argument *resol*:** argument that takes into account the time step used. By default, this parameter is set to 1, which means that all period values (in text files and in graphics) will be given in the unit of the input signal f . However, if one wishes to keep the period values in "days", the value of this argument corresponds to the number of observations present per hour. Thus, for example:

Daily data (Bierset)	$resol = 1$
Data every three hours (Uccle)	$resol = 8$
Hourly data (Bierset)	$resol = 24$
Monthly data (ENSO signals)	$resol = 0.0328767 (= \frac{1}{\text{average number of days in a month}})$

- **Noise argument *per_min*:** the minimum period below which periods are considered as noise. If the resolution argument has been modified, this period must be specified in days. In the context of this work, and more generally in the field of climatology, we consider this period should be set to 90 days. If one does not wish to have a minimum period, for example when detecting daily periods (as in the case of Bierset), it suffices to give a negative value to this argument.

- **Concavity argument** *seuil_concav*: the maximum threshold of the second derivative of the signal at the location of the maximum. Beyond this threshold, the maximum is considered "too flat" to be retained. As we will see later, this argument has been optimized to provide the best possible results.
- **Zone argument** *bande*: an argument modifying the zone in which the period can vary along the time series.

$$\text{Tolerance Range} = |\bar{\xi} - IP_{\text{left}} * \text{bande}| + |\bar{\xi} - IP_{\text{right}} * \text{bande}| \quad (17)$$

As for concavity argument, the value of this argument has also been optimized to obtain the highest quality results possible.

Note that for certain particular periods, we added conditions in the code in order to obtain the most "relevant" zone.

- **Border effects argument** *border_effect*: This takes into account the borders effects when creating graphics and text files. Indeed, only the period values for the initial signal (without the borders effects) are of interest to the user and thus need to be saved. If it is set to 0, WIME considers that no borders effects has been added in the pre-processing. If it is set to 1, WIME considers that the signal has been tripled, as is the case with mirror and periodic effects. Therefore, this is the default value and what we will use in the context of this master thesis.
- **Save argument** (for text files) and **filename** (for text files and figures).

4 Fourth part : Temperature analysis

After reviewing all the necessary theoretical aspects, we will apply the WIME algorithm to a first time series: the Bierset temperatures. This will allow us to understand that the algorithm works, firstly because it enables the reconstruction of the time series and, secondly, because it allows the detection of periods that are explainable by climatic processes

4.1 The Bierset temperature data (1956-2023)

The Bierset weather station is situated 9 kilometers west of Liège’s city centre, on the northern edge of the Meuse valley, at an elevation of 175 meters. The station reports an average temperature of 8°C.

This station recorded an observation every 3 hours (from 1956 to 1981) or hourly observations (from 1981 to 2023).

It should be noted that the different sinusoidal components c_i are by definition centered at 0. Therefore, we subtracted the mean from the temperature observations to achieve consistent results between the model and the reconstruction. We obtained the "centered temperature".

$$\text{Centered temperature} = \text{Temperature} - \overline{\text{Temperature}} \quad (18)$$

4.2 Periods larger than 3 months

4.2.1 Arguments chosen

The centered temperature data for each day was averaged to provide a single value per day (temporal resolution degradation). Thus, the resolution argument is set to 1 (daily resolution). This had little to no impact since we are looking for periods of at least three months (noise argument = 90).

For the zone and concavity arguments, we attempted to employ values that would lead to the most accurate modeling possible. To assess the validity of models, we will use correlation and root mean square error (RMSE) indicators.

If O represents data observed, M represents the reconstructed data, and n is size of the time series, we can calculate these indicator as:

$$\text{Correlation} = \frac{\sum_{i=1}^n (O_i - \bar{O})(M_i - \bar{M})}{\sqrt{\sum_{i=1}^n (O_i - \bar{O})^2 \sum_{i=1}^n (M_i - \bar{M})^2}} = \frac{\text{cov}(O, M)}{\sigma_O \sigma_M} \quad (19)$$

$$\text{RMSE}_{\text{stand}} = \sqrt{\frac{\sum_{i=1}^n (O_i - M_i)^2}{n}} \cdot \frac{1}{\sigma_O} \quad (20)$$

We ran the programme with **zone argument** values ranging from 0.5 std to 3 std (at intervals of 0.05 standard deviations) and assessed the quality of the results. The value that provided the best reconstruction, where the correlation peaked and the

RMSE reached a trough, was 1.4.

We thus retained this zone value and ran the model with different values for the **concavity argument**, spanning different orders of magnitude. It appears that very small concavity values yield the best results. The chosen value for the concavity argument is 0.001 (below this value, no further changes occur). This result means that periods will be selected solely based on their amplitudes.

We applied the mirror effect, which implies that we set the border effect argument to 1.

4.2.2 Reconstruction and validation

It is feasible to aggregate the sinusoidal components (by simple addition) to formulate models capable of "reconstructing" the values of the several indices. We can then naturally compare this "model" to the observations and evaluate its quality.

We compiled models that include from 1 to 15 first periods. As we add components, we observe that the correlation value increases and the RMSE decreases, indicating in both cases an improvement in the quality of the modeling. But the importance of this improvement decreases. This effect, shown in Figure 8, was expected because, given the structure of the code (Section 3.3.2), the added periods are progressively less energetic.

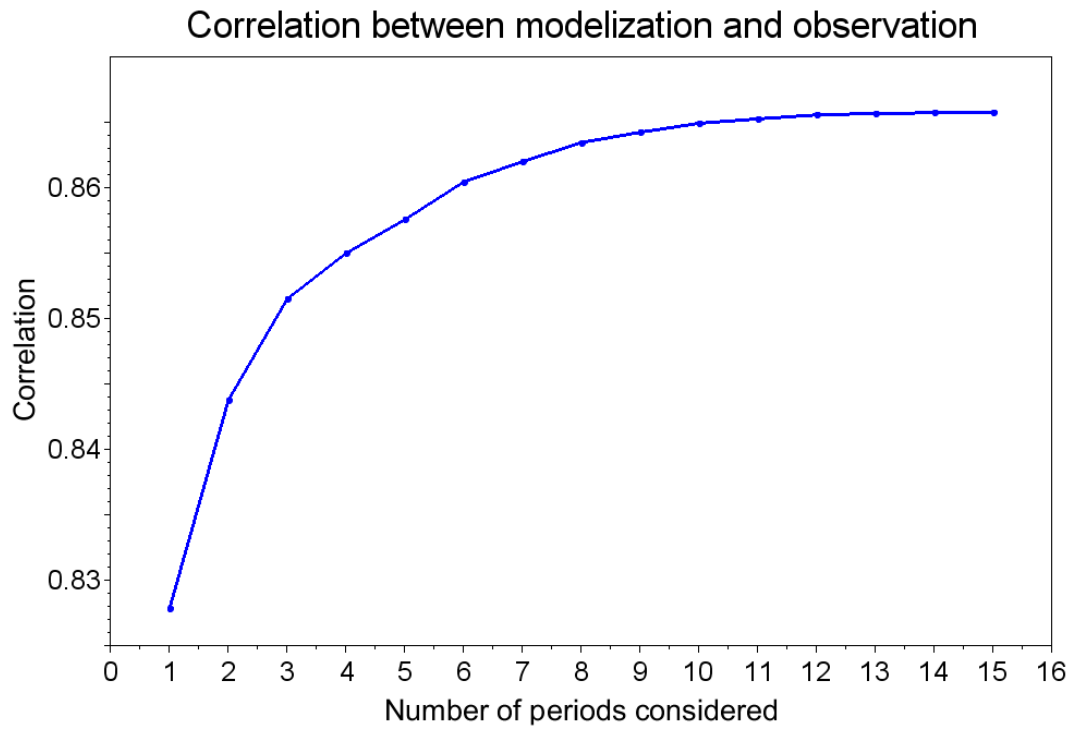
With 6 periods, we reach a **correlation value of 0.86** and a RMSE of 3.14 °C. Even with additional periods, we never reached a 0.87 correlation.

4.2.3 Periods

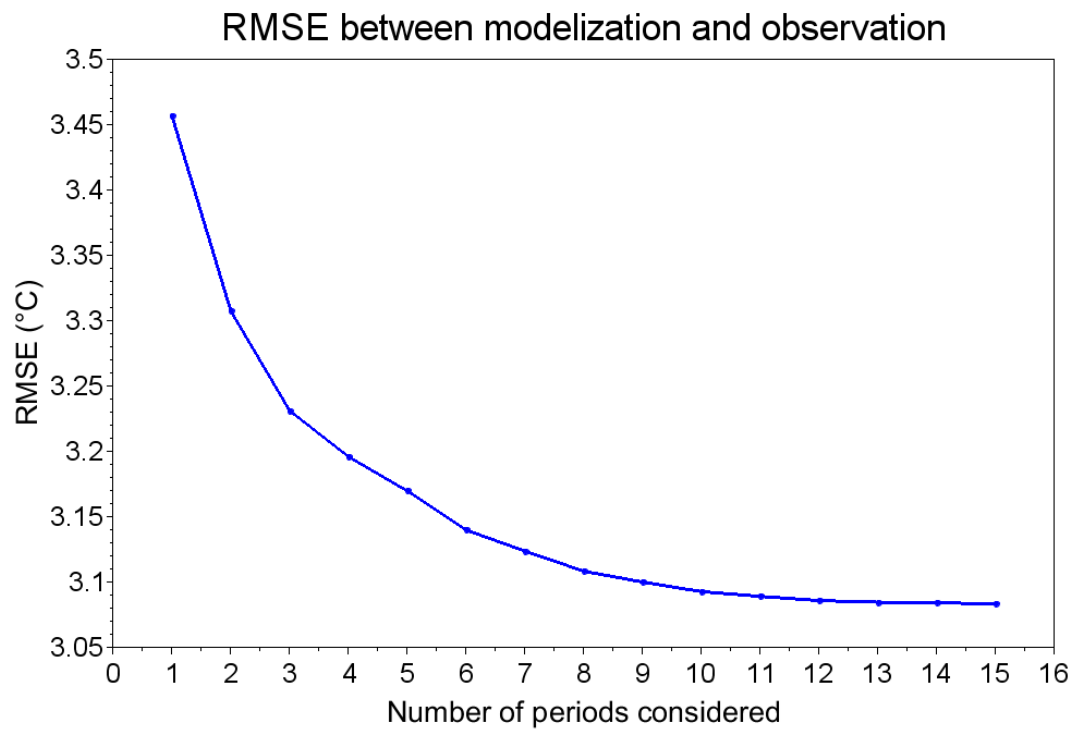
These first 6 periods are represented on the spectra (Figure 9). Certainly, they are classified from the most to the least relevant (based on amplitude).

- **Period 1:** 364.7 days (1 year). This first period is the year and is much more significant than the others. Indeed, its amplitude is equal to 3.57°C, which corresponds to a variation of 7.14°C (twice of the amplitude). It has over 9 times more energy than each of the other periods (taken separately).

This obviously corresponds to the Earth's orbit around the Sun.



(a) Correlation between modelization and observations for Bierset temperature.



(b) RMSE between modelization and observation for Bierset temperature.

Figure 8: General validation of Bierset temperature modelization.

- **Period 2:** 92.8 days (3 months), with a 0.5°C amplitude. This period is at the threshold of the zone considered as noise. We tried to slightly increase the *noise* argument to avoid this period, but it impacted the correlation and RMSE².
- **Period 3:** 188.8 days (6.2 months). It has a 0.4°C amplitude and indicates slightly random variations over time.

To understand the origin of the 12-hour period, we ran the WIME algorithm on an artificial file that simulated temperatures between -1 (sunrise and sunset) and 1 (sun at zenith) for 10 years. The times are the actual sunrise, sunset, and zenith of the sun, which vary throughout the year. Then, the values were interpolated using splines to obtain a value for each hour. Note that, because the file is not expressed in degrees, the amplitude is obviously not comparable to the amplitude of Bierset temperatures.

The initial spectrum of this theoretical file is presented in Figure 10, where we can observe that the 4th period corresponds to 6 months. This indicates that this half-year period in the real observation data can be explain by an ephemeris phenomenon.

- **Period 4:** 913.7 days (2.5 years), with an amplitude of 0.2°C .

It is clear that this corresponds to the 30-month period, as previously discussed by Mabilie **and others** 2012. This is associated with variations in two climate indices: AO (Arctic Oscillation) and the NAO (North Atlantic Oscillation). These indices affect stratospheric advection patterns and, consequently, temperatures. The regions most influenced by variations in the AO and NAO are Europe (where Bierset is located) and Asia, and indeed, these are the areas where this cycle is most clearly observable (Mabilie **and others** 2012; Zhou **and others** 2001).

- **Period 5:** 2329.2 days (6.4 years): this period varies from 5 to 7.8 years.
- **Period 6:** 262.4 days (8.6 months): this period varies from 6 to 11 months.
- **Period 7:** 8 659 days (23.7 years): this seventh period is also discussed here because it has a similar amplitude value (0.2°C) and also, it can have a physical

²The correlation falled at 0.84 and RMSE was blocked at 3.3°C

explanation. This cycle varies between 18.8 to 25.3 years. It could be more since 25.3 years is the maximum period detectable for this length of time series given to WIME in this simulation).

Indeed, it is related to solar activity, that follows a well-known 11.2-years cycle. However, every 11 years, the polarity reverses, leading to a complete cycle of approximately 22 years, which could correspond to this seventh period (NASA 2011; Mabilie 2014).

4.3 Daily periods

The WIME program was run with hourly temperature data. Thus, before 1981, a linear interpolation was performed to increase the temporal resolution from 3 hours to 1 hour.

Regarding the arguments, we chose the same ones as for longer periods, except that we did not set a minimum period (noise argument = -1), and the resolution argument was naturally set to 24.

The only two daily periods found using this methodology are:

- 24 hours: This period has an amplitude of 0.76°C , which is nearly 5 times less than the annual period. It is actually the second most significant period. It obviously corresponds to the Earth's rotation.
- 12.2 hours: This period has an amplitude of 0.23°C , so 15 times less than the annual period.

This half-day period should correspond to a similar effect as the 6-months period (see Section 4.2.3). Indeed, a 12-hours period also emerges in the theoretical file (third period on Figure 10).

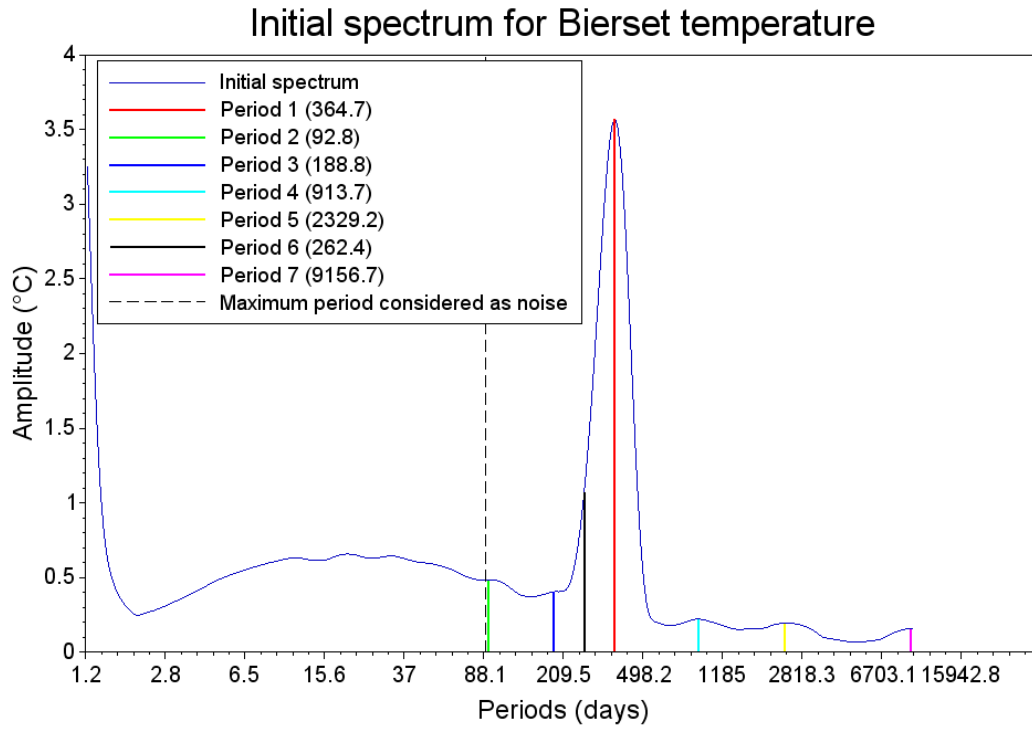


Figure 9: Spectrum of the Bierset temperature.
Vertical solid lines show main periods.

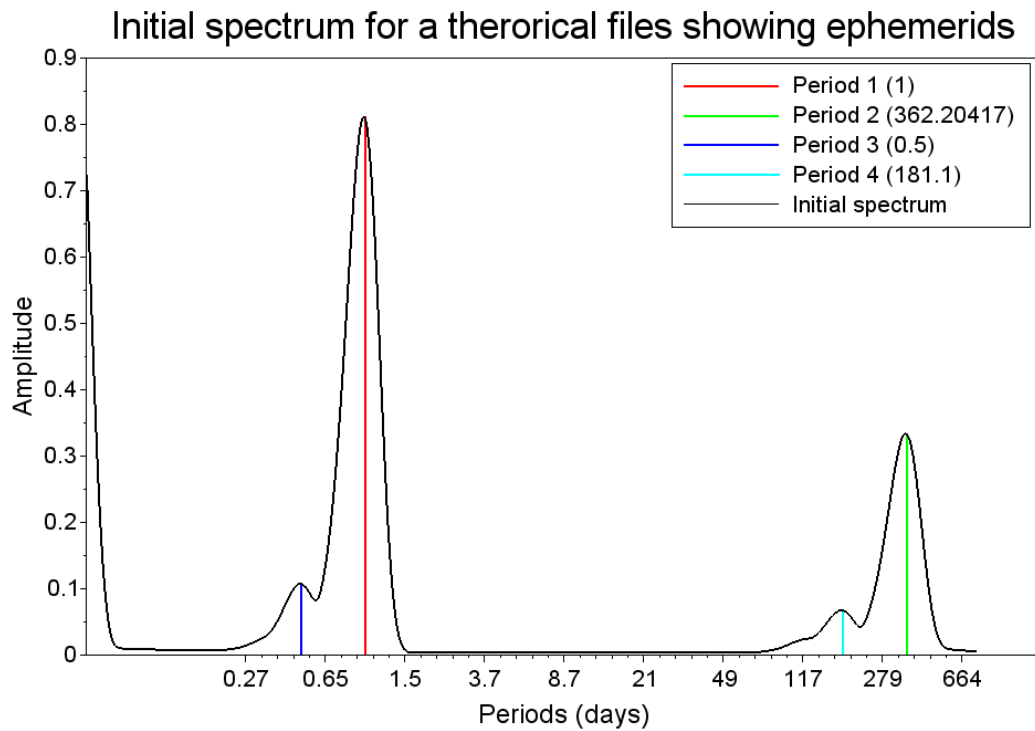


Figure 10: spectrum of artificial temperature, ranging from -1 (sunrise and sunset) to 1 (sun at zenith)
Vertical solid lines show main periods.

5 Fifth part: ENSO signal analysis

Since WIME works on temperatures, we will apply it to two indices that characterize the ENSO phenomenon: one focusing on the oceanic component, and the other on its atmospheric component.

We will reconstruct these two indices and evaluate the quality of the reconstructed signal. Special attention will be paid to how the two phases (Niño and Niña) are reported.

Moreover, a description of the different periods will be made, considering their evolution (in frequency and in amplitude).

5.1 Different time series (1951-2023)

Two databases were used: the Oceanic Niño Index (ONI) and the Southern Oscillation Index (SOI). These indices are the most commonly used to describe the phenomena of "El Niño" and "La Niña", which we will consider as canonicals. Both databases cover the same period (from 1951 to 2023). Conducting a parallel analysis of these two databases is noteworthy because they correspond to two distinct methodologies for illustration of the ENSO phenomenon.

- **ONI** (Figure 12a): This corresponds to an anomaly of the sea surface temperature in the Niño 3.4 region (shown in Figure 11), with the base period reflecting a 30-year average. This region extends from 170°W to 120°W and from 5°S to 5°N and can be considered as a measure of the "oceanic component" of the ENSO phenomenon (NOAA 2024b).

This anomaly is calculated monthly, and a 3-month running mean is then applied (NOAA 2024b).

NOAA defines this index and allows for easy identification of whether the system is in the "El Niño" or "La Niña" phase. If the indicator is greater than 0.5 (corresponding to a SST above 28°C, and thus to the expansion of the Warm Pool) for at least 5 consecutive months, it is considered the "El Niño" phase. The "La Niña" phase occurs when the indicator is less than or equal to -0.5 for at least 5 consecutive months. The data naturally come from the NOAA website (NOAA nodate; NOAA 2024b).

- **SOI** (Figure 12b): This corresponds to a comparison between the sea-level pressure in Tahiti (Pacific) and in the city of Darwin (Australia). The locations are also highlighted in Figure 11. It can be considered as a measure of the "atmospheric component" of the ENSO phenomenon.

The two SLPs are normalized with respect to the base period 1981-2010 (NOAA 2024c).

$$SOI = \frac{SLP_{Tahiti, standardized} - SLP_{Darwin, standardized}}{\sigma_{monthly}} \quad (21)$$

In this master thesis, anomaly values have been considered, relative to the same base period.

Figure 12b shows that this index is much more noisy than ONI.

Note that SOI is negatively correlated with ONI. Indeed, prolonged negative values of this index indicate a positive anomaly in Darwin. In other words, it means we can have anticyclonic conditions in Oceania, and so is an El Niño situation. On the other hand, prolonged positive values indicate La Niña (depression on Darwin). There is no precise value, neither for this prolonged period nor for the threshold values to consider that we are transitioning into an El Niño or La Niña event. The data also come from NOAA (NOAA nodate; NOAA 2024c).

To facilitate a comparison between the results of the two signals, we will take the inverse of the SOI signal (as in Figure 12b). Thus, the two signals will be directly correlated, and positive (resp. negative) values will correspond to El Niño (resp. La Niña) events.

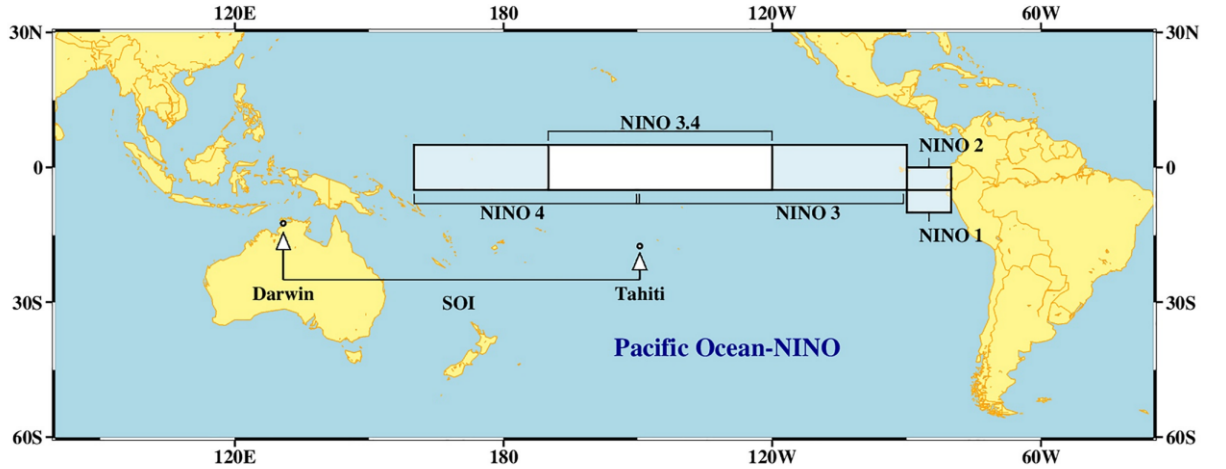
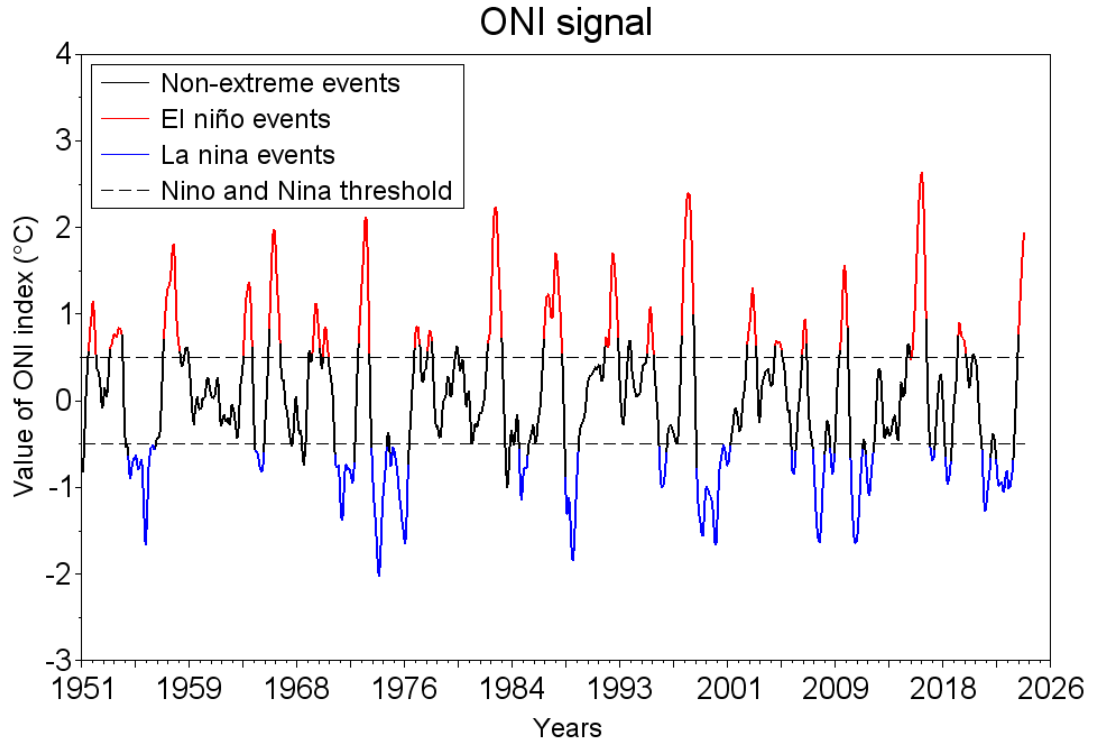


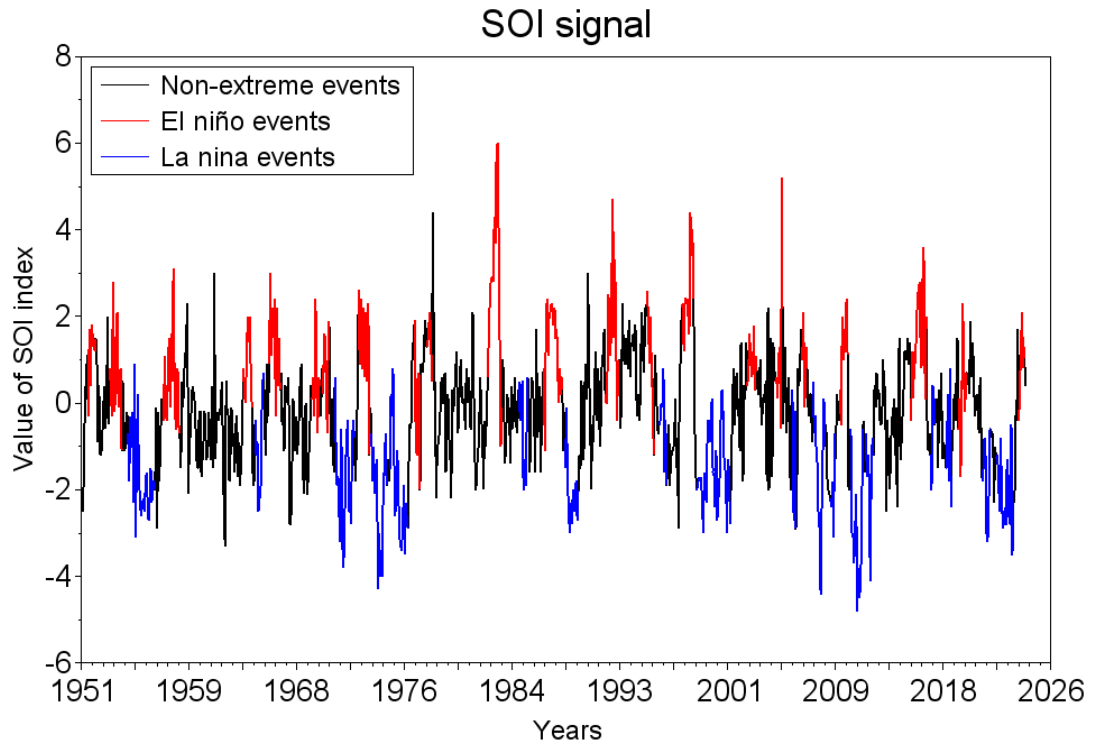
Figure 11: Location of the Niño 3.4 region, Darwin and Tahiti (N. Yu **and others** 2021).

The correlation between the ONI and SOI (reversed) is equivalent to 0.73.

To define whether a period was an El Niño or a La Niña situation, we will use the ONI definition (5 consecutive months above or below 0.5°C). These moments should be identical for both signals since they account for the same phenomenon. In Figures 12a and 12b, it is specified whether it is a "non-extreme" (ENSO-neutral), "El Niño", or "La Niña" situation. The sum of the 3 situations equals the total indices database (875 months, so 72 years). This information is summarized in Table 1.



(a) Value of ONI index.



(b) the inverse of the value of SOI index.

Figure 12: ENSO indices on from 1951 to 2023. Red (resp. blue) curves represent El Niño (resp. La Niña) periods, based on ONI criteria.

Following what was seen in the theoretical section (Section 2), La Niña periods are on average longer (1 year) than El Niño periods (9 months), and this effect seems even more significant when analysing the graphs. Indeed, we can see that El Niño periods appear more often as strong, singular peaks, whereas La Niña events are less important but generally multi-peaked. This is consistent with the nonlinear nature of the ENSO phenomenon and the "Multiyear La Niña" events detailed in the theoretical (Section 2).

Situation	number of events	Average length
El Niño event (red curves)	23 events (215 m. or 25% of the database)	9.3 months
La Niña events (blue curves)	19 events (229 m. or 26% of the database)	12.1 months
ENSO-Neutral or non-extreme (black curves)	431 m. or 49% of the database	/

Table 1: Occurrence and period length for the different ENSO situations

5.2 Arguments chosen

Similarly to temperature analysis (Section 4.2), the **resolution argument** is set to 0.0328767, which corresponds to $\frac{1}{\bar{d}}$, where \bar{d} is the average number of days in a month, and the **noise argument** is equal to 90 (this still corresponds to 90 days given the change in resolution argument).

Then, we optimise again the concavity and the zone arguments, with the same methodology as for temperature. It is particularly relevant to do it in these part because changes in these arguments create a bigger gap in the results for ENSO indices than for temperature data.

When using at least 2 components, the analyses reveal a noticeable degradation in modeling precision for both the smallest and largest **zone argument** values. Within this range, there exists a plateau where the quality experiences minimal variation with changes in the argument value. However, the position of this plateau varies depending on the index (ONI or SOI) and the number of periods considered. To maintain consistency in the results, it will be necessary to consider a value of the zone argument that ensures good quality regardless of the ENSO index, the periods, or even the statistic index (RMSE or correlation) considered.

Between 1.25 and 1.6, it seems that there is a plateau regardless of the case considered.

We opted for a value situated at the midpoint of this range, specifically, a zone argument of **1.425**.

Afterward, we retained again this zone value and ran the model with different values for the **concavity argument**. An initial observation is that the quality steadily deteriorates when this argument is >1.6 and when it is <0.05 . Between 0.05 and 1.6, the quality fluctuates. Two plateaux of higher performance are observed: between 0.05 and 0.5 and between 0.8 and 1. We have therefore chosen to assign a value to this argument at the centre of the larger plateau, namely a value of **0.275**. Thus, unlike temperatures, taking into account the concavity of the peaks enhances the modeling.

Finally, the mirror effect has been implemented (and the border effect argument was set to 1).

5.3 Reconstruction and validation

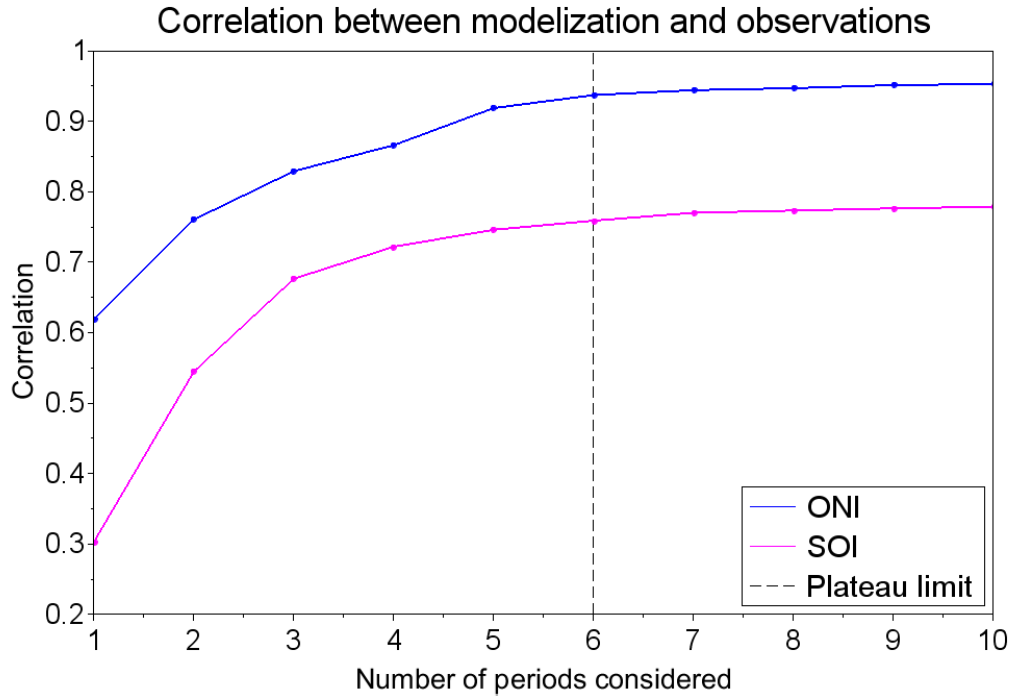
5.3.1 General validation

Firstly, we will identify which periods play the biggest roles in the reconstruction of these two indices (ONI and SOI). Notably, Figure 13 illustrates their contributions using the statistical indicators of correlation (Equation 19 for Figure 13a) and RMSE (Equation 20 for Figure 13b).

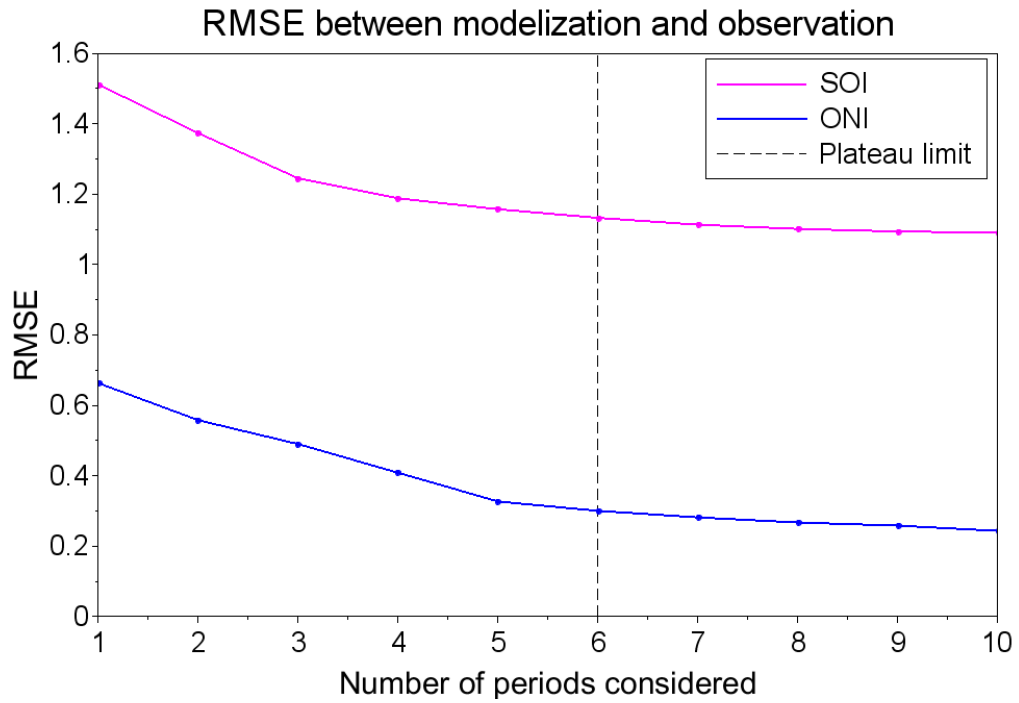
As we add components, we observe that the correlation value increases and the RMSE decreases, indicating in both cases an improvement in the quality of the modeling. Note that this increasing with periods adding is really important. This indicates that the phenomenon is complex and that multiple periods are crucial for its explanation and prediction, in contrast to temperatures, where the annual period alone could explain the majority of the temporal evolution.

The graphs of Figure 13 highlight that the first six periods contribute the majority of the information and a "plateau" formation is observed for the subsequent periods (after the black dotted line on Figure 13).

Therefore, for the remainder of this work, we decided to include only the first six periods in the modeling. The values of these indicators are listed in Table 2, which shows that the ONI index is much better modeled than the SOI index.



(a) Correlation between modelization and observations for ENSO indexes.



(b) RMSE between modelization and observation for ENSO indexes.

Figure 13: General validation of ENSO indices modelization. Blue curves refer to the ONI index while pink curves refer to the SOI index. Black dotted lines show the start of the plateau.

ENSO Index	Correlation	RMSE
ONI (based on SST)	0.94	0.29 °C (standardised 0.35)
SOI (based on SLP)	0.76	1.33 (standardised 0.65)

Table 2: Correlation and RMSE between modelization (with the first 6 periods) and observations of ENSO indices

The reconstruction models are presented by the blue (for ONI) and red (for SOI) curves in Figure 14. When compared to the observational data (black lines), we observe a strong alignment. In most cases, the peaks are underestimated, meaning that the strength of the events is modeled as being less intense than they actually are.

5.3.2 Extreme events validation

We calculated the correlation value and RMSE by separating the databases based on the Pacific situation (Table 4). This resulted in three new restricted databases: one comprising solely ENSO-Neutral months, another containing "El Niño" months, and a third consisting of "La Niña" situations.

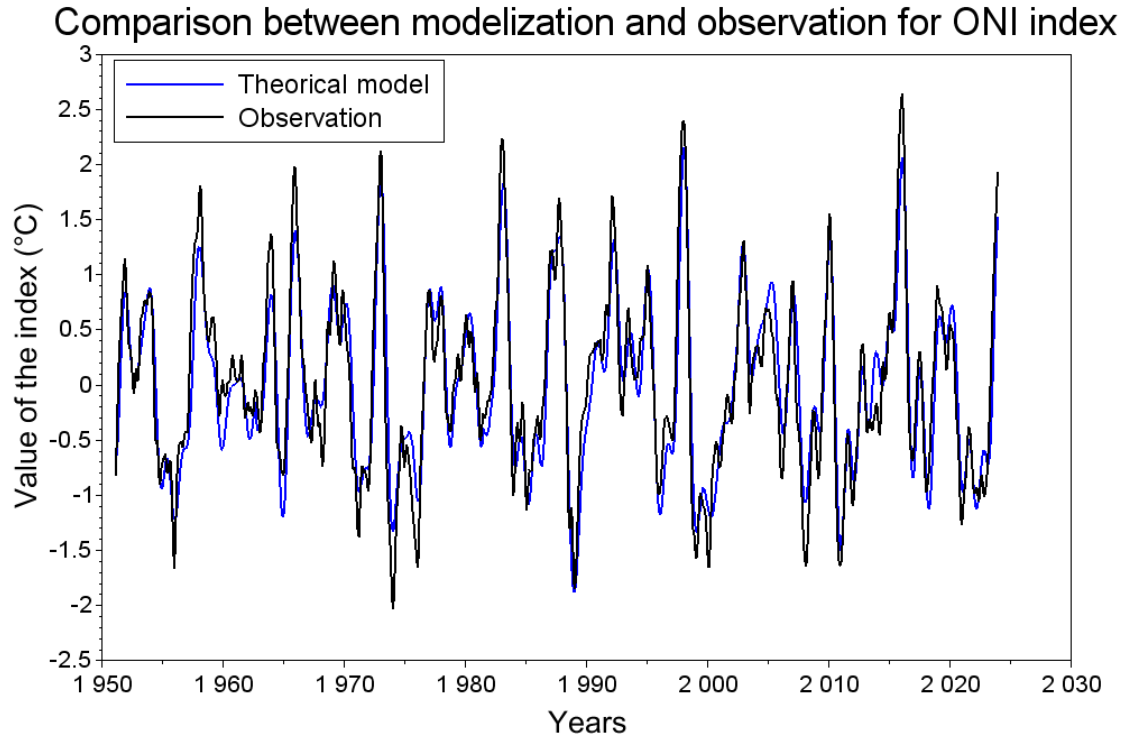
We can observe a significant reduction in correlation compared to the complete

Database (ONI)	Correlation	RMSE
El Niño (Red curves on Figure 12a)	0.85	0.32°C
La Niña (Blue curves on Figure 12a)	0.71	0.29°C
ENSO-Neutral(Black curves on Figure 12a)	0.74	0.28°C
Complete database (previously mentioned in the table 2)	0.94	0.29°C

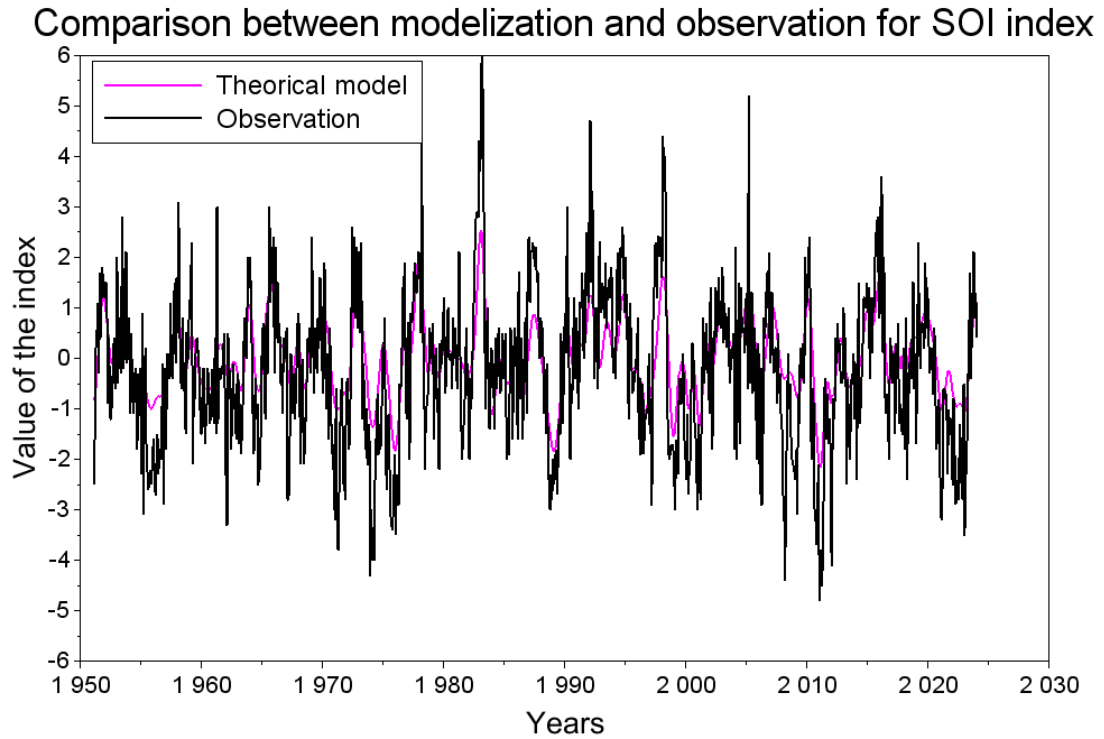
Table 3: Correlation and RMSE between modelization (with the first 6 periods) for ONI signal depending on the ENSO situations (ONI criteria).

database. This can be simply explained by the intrinsic normalization in the correlation formula, leading to a decrease in correlation for small databases.

Regarding correlation, we can see that El Niño events are the best modeled, while performance is weakest during La Niña situations. Concerning the RMSE, it is similar for all ENSO situations, although it is slightly higher for El Niño events. This could be explained by the larger peaks for Niño situations in the ONI database, which the model often tends to underestimate.



(a) ONI index.



(b) SOI index.

Figure 14: Comparison between modelization (first 6 periods) and observations for ENSO indices. Black curves stand for observation and coloured curves stand for models data.

For the SOI signal, we observe the same effect of decreased modeling quality with database separation. The correlation values on the complete database, already lower than for ONI, reach very low values. Correlation is significantly better during events (El Niño and La Niña), while RMSE is higher. This can again be explained by the same effect of peak underestimation.

Database (SOI)	Correlation	RMSE
El Niño (Red curves on Figure 12b)	0.59	1.17
La Niña (Blue curves on Figure 12b)	0.60	1.34
ENSO-Neutral(Black curves on Figure 12b)	0.48	0.98
Complete database (previously mentioned in the table 2)	0.76	1.33

Table 4: Correlation and RMSE between modelization (with the first 6 periods) for SOI signal depending on the ENSO situation (ONI criteria).

Another approach would be to focus solely on the binary detection of an event (El Niño or La Niña), using the same ONI criteria³. The efficiency is given by the formula below:

$$Efficiency = \frac{True\ Positive + True\ Negative}{Complete\ database} \quad (22)$$

The efficiency is 0.90 for El Niño events and 0.89 for La Niña events.

The remaining 10-11 percent is distributed between "false negatives" (events observed but not modeled) and "false positives" (events modeled but not observed), as quantified in Table 5.

Events (ONI)	El Niño	La Niña
False negative	4% (35 months)	4% (54 months)
False positive	6% (37 months)	7% (58 months)

Table 5: Occurance of "false positive" and false negative" for ONI modeled index

Table 5 also reveals that there are more false positives than false negatives, indicating that the model tends to overestimate the number of ENSO events (both Niño and Niña). This might seem counterintuitive given that we stated previously that the model causes an underestimation of the peaks. The explanation for this surprising

³There is no sense in doing SOI because of the ONI criteria chosen for determine Niño and Niña events

result is that the model actually overestimates the duration of the events rather than their number (see Table 6).

Events (ONI)	El Niño	La Niña
Observed number of events	23	19
Predicted number of events	23	17
Observed average length event	9.3 months	12.1 months
Predicted length event	10.2 months	14.7 months

Table 6: Occurrence of "false positive" and false negative" for ONI modelized index

For El Niño situations, the model predicts as many events as were actually observed. It thus predicts an average duration of 10.2 months (compared to 9.3 months for the observations). For La Niña situations, the model predicts fewer events than those observed, which increases the average duration of the event to 14.7 months, which could correspond even more closely to reality according to the literature.

If we consider event detection as a whole, that is, if we look at whether the model detected an El Niño occurrence at the time it was observed, without accounting for a potential difference in the length of the event, the model based on the ONI index detects all El Niño events. Specifically, there is one false positive in the entire dataset, which is compensated by the fact that the model joins two events (which were separated in the observations). Regarding La Niña events, there are actually 3 false negatives and 1 false positive when considering the events as a whole.

5.4 Periods

We extracted the first periods of these indices. These periods and their amplitudes vary significantly over time (unlike the temperature periods, see Section 4.2).

Through approximations, one can identify consistent periods irrespective of the ENSO index calculation method. It is worth emphasising, however, that the algorithm does not attribute equal "relevance" to these periods. Hence, the period lengths appear to match (Table 7). Moreover, periods that we can observe in only one index (B and F lines in Tab 7), are the sixth periods, so one of the less relevant.

It should be noted that we also included the 7th periods in this table, even though they were located after the plateau (and had very low energy), because they fit with other more energetic periods.

Approximate period	Mean peak periods for ONI	Mean peak periods SOI
A. 12.5 years (low)	Period 4 (148.1 months)	Period 1 (150.7 months)
B. 9 years (low)	Period 6 (108 months)	/
C. 4.0-6.50 years (mid)	Periods 3 + 7 (62.3 and 58.1 months) Period 1 (44.0 months)	Periods 5 + 7 (78.0 and 47.2 months) Period 3 (53.3 months)
D. 2.5 years (high)	Period 2 (27.1 months)	Period 2 (29.6 months)
E. 1.4 (high)	Period 5 (16.7 months)	Period 4 (17.6 months)
F. 1 year (high)	/	Period 6 (12 months)

Table 7: Period in ENSO indexes, generated by WIME

All periods over 7 years will be considered "low frequency." Those between 3 and 7 years will be referred to as "mid-frequency," and those less than 3 years will be classified as "high frequency."

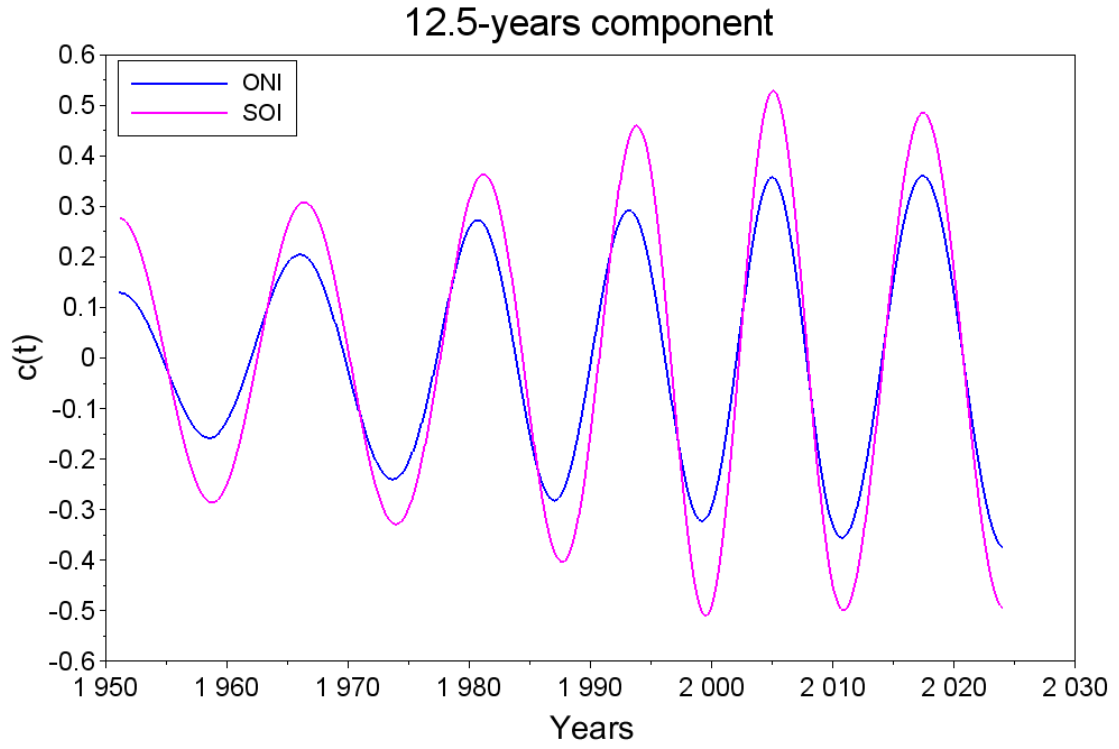
If we analyse how mid-frequencies period evolve along the time series (C in Tab 7), the best combination seemed to assimilate period 1 (ONI) to period 3 (SOI) on the one hand, and the sum of the two other mid-frequencies periods on the other hand, after exploring all possibilities.

5.4.1 Low-frequency period

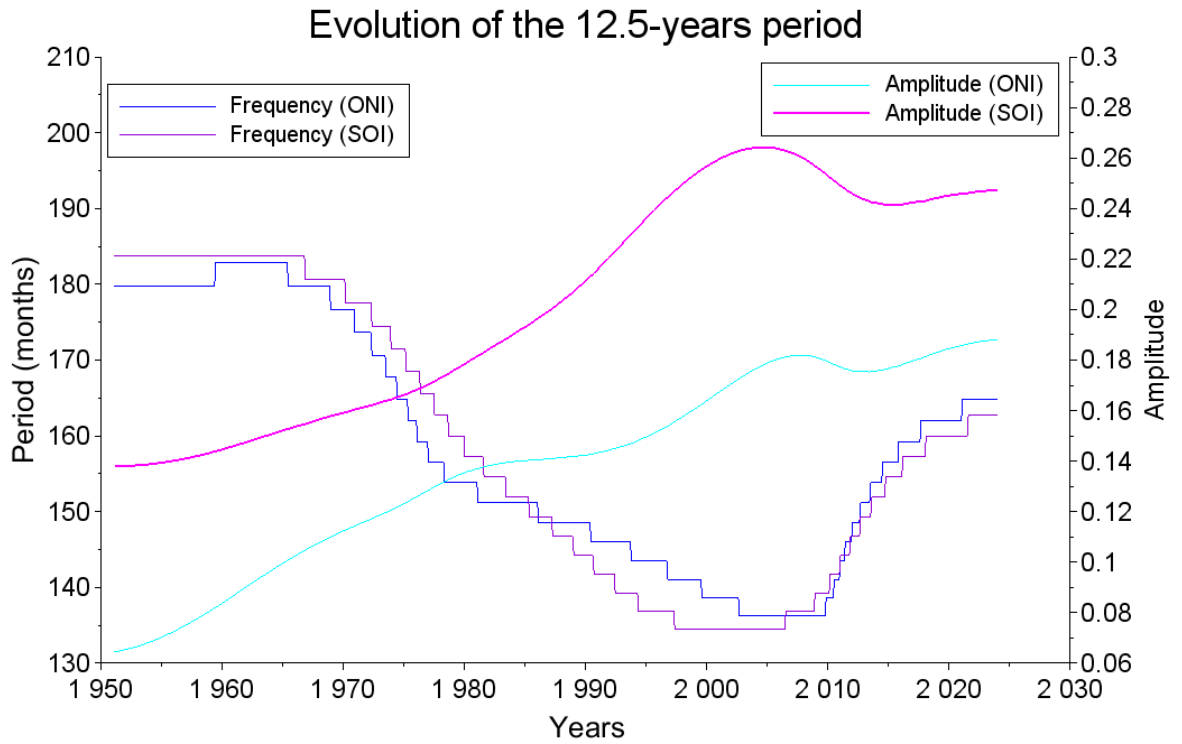
The lowest frequency period is around 13 years (row A in Table 7). Figure 15 shows how it evolves over time. A primary observation reveals the remarkable similarity in values and behavior between the two components. They exhibit near-perfect phase alignment (Figure 15) and demonstrate an almost identical evolution in frequency and amplitude.

Concerning frequencies, both peak around the 1950s at a value of approximately 182-184 months. following this, there is a relatively steady decline until 1997 (for SOI) and 2002 (for ONI), until the value of 134-136 months is reached. Finally, a renewed increase is observed, reaching the current value of 162-165 months. Consequently, the period has fluctuated between 11 and 15 years (mean of 13.25 years, and mean peak period of 12.5 years) for the entire time series.

Furthermore, it is notable that both indices exhibit an increasing amplitude over time (accentuated in the years 2000s). It has nearly doubled for the SOI signal, and almost tripled for the ONI signal. This effect contributes to increasing the strength of El Niño and La Niña events.



(a) Representation of the component.



(b) Evolution of the amplitude and the frequency.

Figure 15: Evolution of the 12.5-years components for ENSO indices. Dark blue and light blue curves refer to ONI signal while purple and pink curves refer to SOI signal

Finally, we can mention the 9-years period for the ONI signal (Figure 16), which oscillates between 95.5 months (almost 8 years) and 119 months (almost 10 years). The amplitude varies significantly. It decreased until 1986, by a factor of 7, before re-increasing until now.

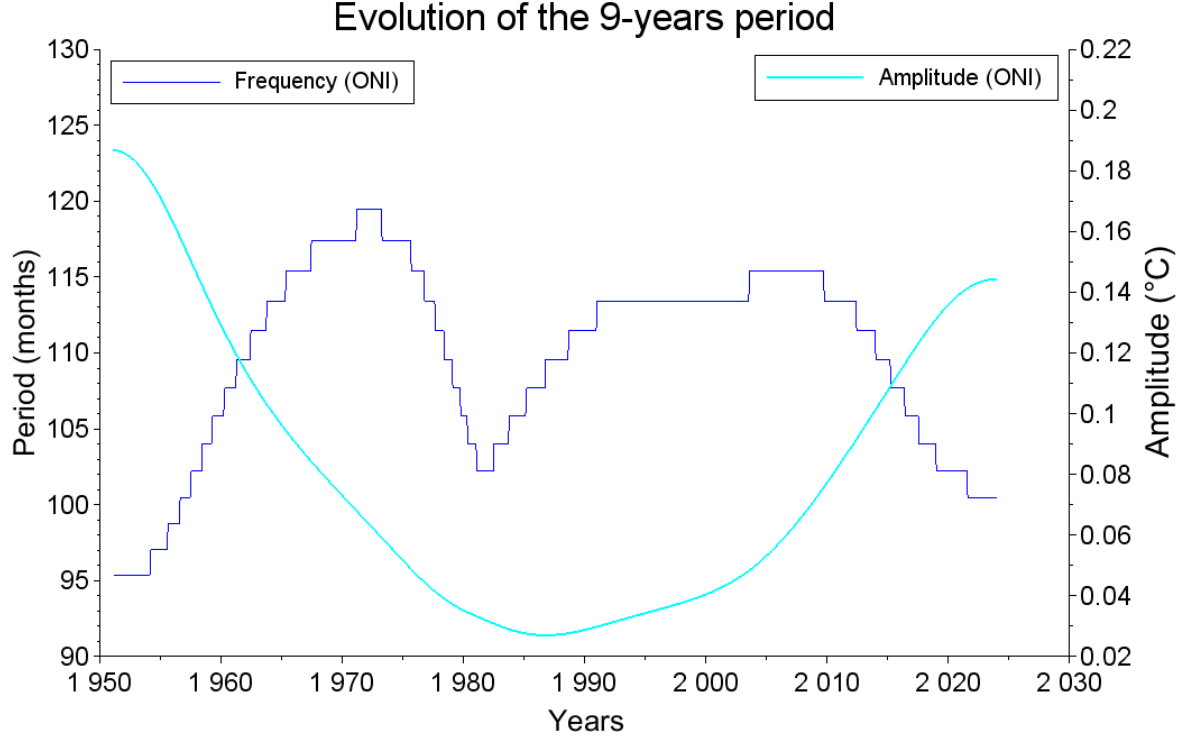


Figure 16: Evolution of the frequency and the amplitude of the 9-years component for the ONI indices.

5.4.2 Mid-frequency periods

The sum of the periods (row C in Table 7), shows that the two indices had a similar and stable period between 1960 and 2000, around 10.5 years (which indeed corresponds to the sum of the two periods considered in Table 7).

Before 1955 and after 2000, this combination of two periods deviates from this average value. It decreases for ONI (down to 9 years) and increases for SOI (up to 12 years). This explains the phase shift of some components before 1955 and after 2000 between the two indices (Figure 17). The amplitude varies from simple to triple and is maximal in the 1950s, 1960s, 1990s, and 2000s for both indices. This can also be seen in Figure 17.

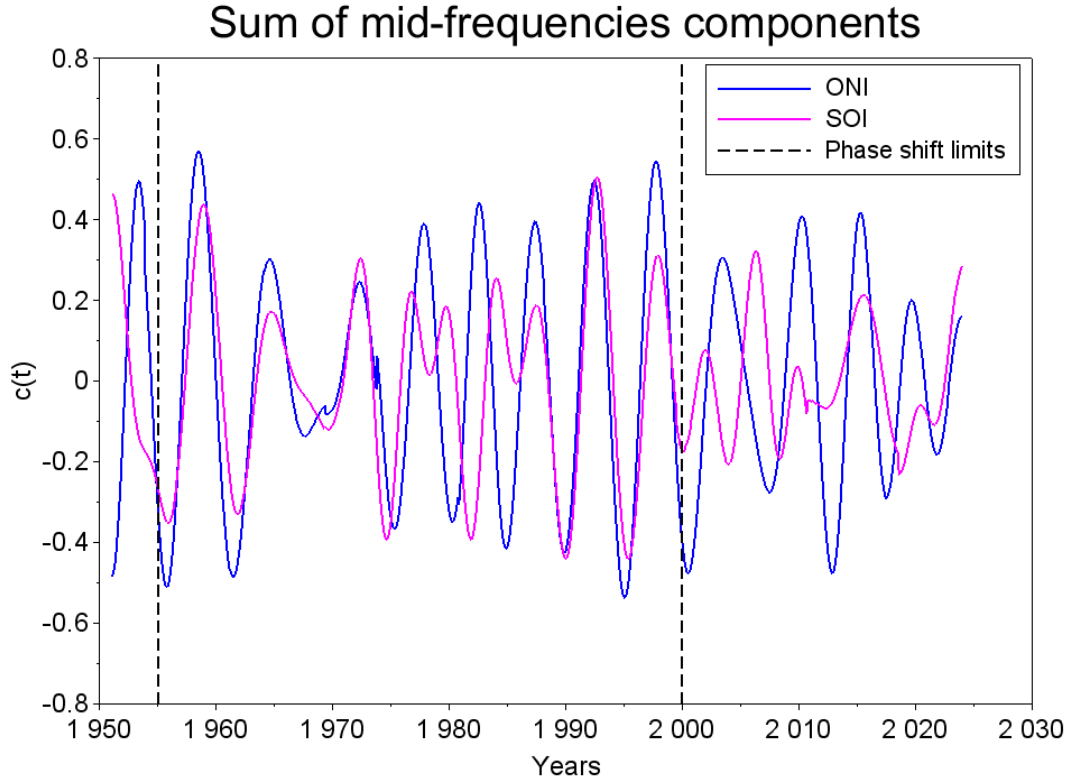


Figure 17: Representation of the combination of two mid-frequencies periods or ENSO indices. Blue curve refer to ONI signal while pink curve refer to SOI signal. Black dotted lines represent the zone where the phase differ between the ONI and SOI signals.

Regarding the single mid-period (second line of row C in Table 7), the two indices experience large oscillations in periods (by a factor of 1.5) and amplitudes (by a factor of 4). Oscillations are more frequent for the ONI index.

5.4.3 High frequency periods

For both the ONI and SOI signals, two high-frequency periods are consistently observed: one around 1.4 years (row E in Table 7) and the other around 2.5 years (row D in Tab 7).

Regarding the 2.5-year period, it takes periods value between 2 and 3 years. The variations in amplitude and in frequencies are quite similar between the two signals, but too numerous to be perfectly identical. The two signals are generally in phase (Figure 18). This is a really important period, for both WIME (2nd most relevant periods for both indices) and the literature (Bruun **and others** 2017; Jajcay **and others** 2018).

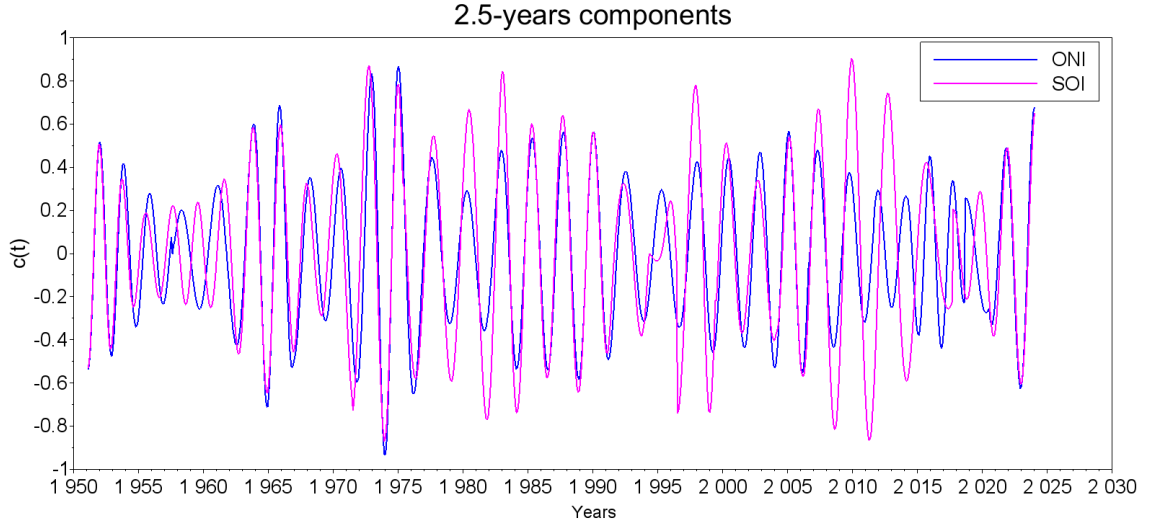
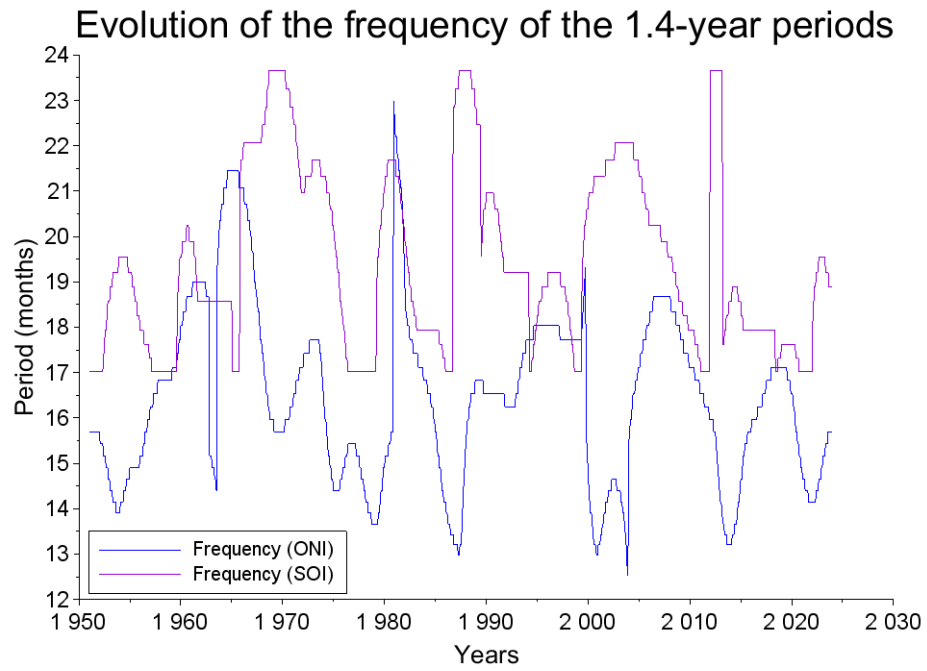


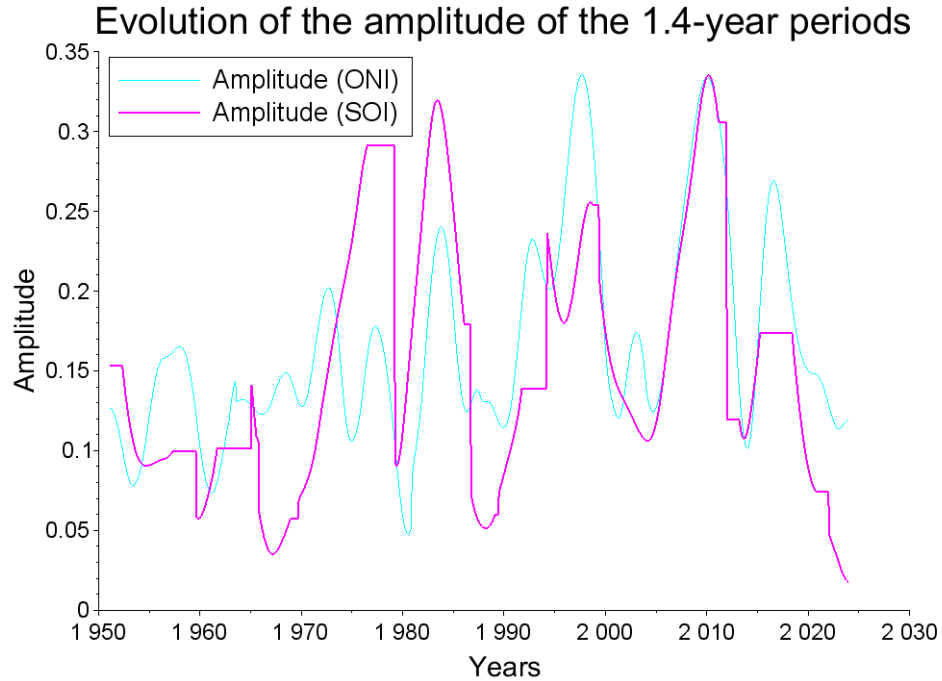
Figure 18: Representation of the 2.5-years component. Blue curve refer to ONI signal while pink curve refer to SOI signal.

For the 1.4-year period, it takes a value between 1 and 2 years. The frequencies of ONI are consistently slightly lower than those of SOI. The frequencies exhibit smaller variations (up to a maximum of 1 year) but are more numerous than lower frequencies (Figure 19a). Amplitudes varied significantly throughout the time series (Figure 19b).

Finally, we can mention the annual period for SOI, which varies significantly and frequently in amplitude.



(a) Evolution of the amplitude.



(b) Evolution of the amplitude.

Figure 19: Evolution of the 1.4-years period for ENSO indices. Dark blue and light blue curves refer to ONI signal while purple and pink curves refer to SOI signal

6 Sixth part: Predictions

In this section, we will make a short- and medium-term future predictions of the ONI index (up to 2-3 years).

Firstly, we will detail the extrapolation methods. Secondly, we will validate the method by performing numerous extrapolations on past data. Finally, we will present predictions of the ONI index up to 2027.

6.1 Method

In the algorithm description, we stated that the components were created using the formula 16, rewritten below:

$$c_i(t) = 2|A_i^*(t)| \cos[\arg W_i^*(t)]$$

The method involves extrapolating both the amplitudes A_i^* and the arguments $\arg W_i^*$ of the various cosine components c_i for time steps t that extend beyond the initial length of the models, and consequently the observations, presented in the previous section. These extrapolated values are then reintegrated into the formula to obtain an extrapolated version of each component c_i .

Predictions of the ENSO index will simply be the sum of these extrapolated components c_i .

6.1.1 Amplitude extrapolation

In the new version of WIME, amplitudes for each component and each time point (month) in the time series can be directly extracted as a text file. Specifically, we extract A_i^* for all t and i . This signal will then be linearly extrapolated.

First, the final segment of each selected amplitude signal was determined. Two criteria were tested to define which part was considered as the "final segment of the signal":

- From the last **extremum** to the last model value
- From the last **IP** to the last model value

After observing the extrapolations, the IP criterion appeared to be the most effective. Therefore, we used this criterion for all amplitude signals.

Next, a simple linear regression was performed, resulting in:

$$A_i^*(t) = m t + p \tag{23}$$

where p is chosen so that the model amplitude value coincides with the amplitude regression value at the last model value. Only values of t greater than the length of the model will be retained.

Finally, to prevent excessively high amplitude extrapolations, the value of A_i^* will be capped if it exceeds the maximum amplitude ever calculated by the model (since 1951); and floored if it falls behind the minimum calculated. Simulating a decrease at this stage would not be relevant due to the high uncertainties.

An example is shown in Figure 20.

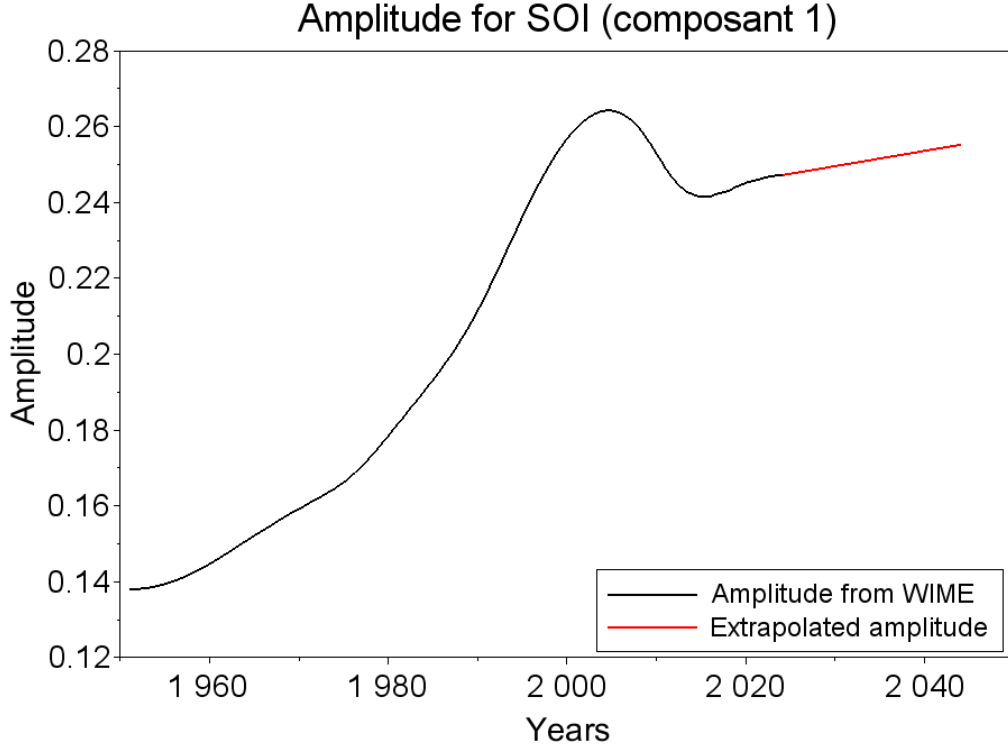


Figure 20: Evolution of the amplitude for 1st SOI component c_1 (black), with 20 years extrapolation (red)

6.1.2 Argument extrapolation

Similarly, we extract the signal $\arg W_i^*$ for all t and i , but the extrapolation method differs.

This signal ranges between $-\pi$ and π , corresponding to the minima of the cosine component ⁴. If the period and phase were stationary, the signal would exhibit a constant slope between $-\pi$ and π over a time interval of one period, then reset to $-\pi$ to start a new cycle.

⁴Minima positions are at π and $-\pi$ because $\cos(-\pi) = \cos(\pi) = -1$; maxima are at 0 because $\cos(0) = 1$

For extrapolation, we create this kind of **sawtooth function** by using the positions of the two previous minima (at $-\pi$ and π) to determine the slope. Consequently, the period and phase values will match those of the last complete cycle (between two minima) observed in the model data and remain the same for all of the extrapolations

An example is shown in Figure 21. The irregular changes in periods and phases between 1951 and 2023 (blue) are clearly visible, followed by a regular sawtooth function for the extrapolation (red).

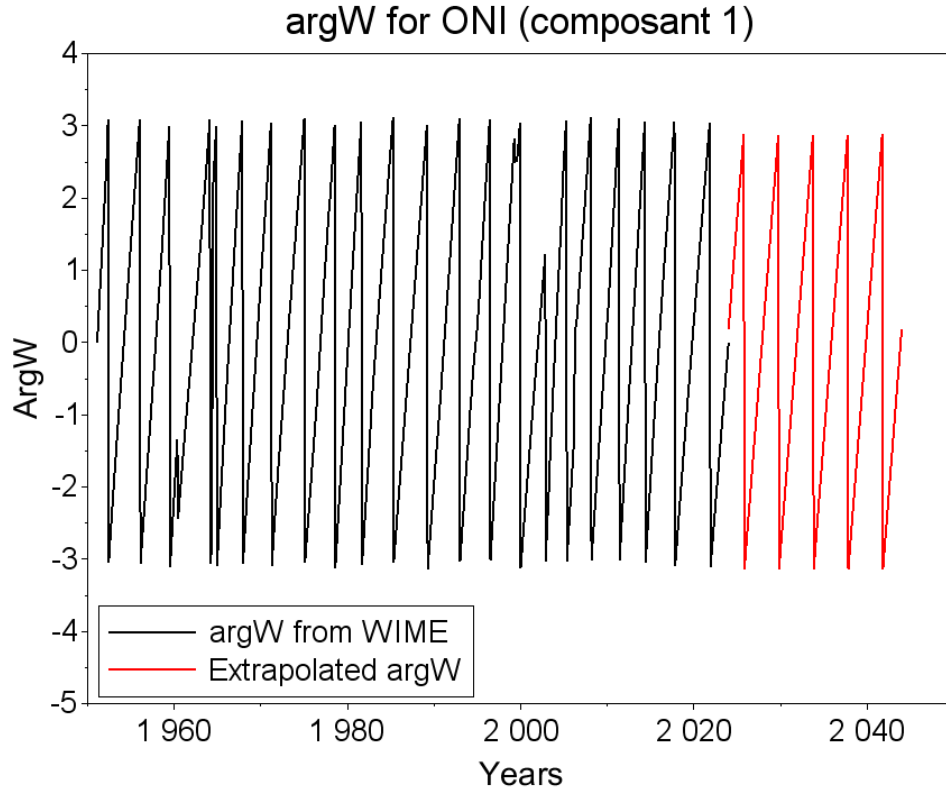


Figure 21: Evolution of the argument for 1st ONI component c_1 (black), with a 20 year extrapolation (red)

6.2 Validation

To validate this method, we will shorten the time series to perform the extrapolation algorithm on already elapsed years (i.e. before 2024). This allows us to compare an observed signal with an extrapolated signal for the same moment.

However, the quality of the extrapolations varies considerably depending on where

the time series is truncated. To generalise, all possible truncations starting from 1981 were considered (a total of 504 simulations). 1981 was chosen to ensure that all periods had experienced at least two complete cycles, enabling the extrapolation algorithm to operate fully.

For each of these simulations, we compared the extrapolation with the observations at each time step over 20 years of extrapolation. The **average of these 504 simulations** is presented in Figure 22, which illustrates two types of results:

- **Difference** (dotted curves in Figure 22): This indicator corresponds to the difference between extrapolated and observed data.

$\forall j \in [1 : 240]$, corresponding to the number of months elapsed since the start of the extrapolation, we have:

$$Difference_j = \frac{\sum_{i=1}^{504} Extrapolated_{i,j} - Observation_{i,j}}{504} \quad (24)$$

i corresponds to the different simulations. By averaging, I eliminate i , resulting in an "instantaneous bias" value (but averaged over all simulations) for each j . A negative value indicates an underestimation of the extrapolated values, while positive values reflect an overestimation.

For SOI (pink dotted curve), a trend of underestimating the indicators becomes evident, which worsens as the extrapolation extends further. More detailed analysis shows that the extrapolation tends to underestimate the magnitude of El Niño and La Niña events, consistent with the findings discussed in the previous section (5.3).

Conversely, for ONI (blue dotted curve), the indicator remains close to zero, ranging between -0.7 and 0.7°C for the first 10 years of extrapolation. This suggests that errors are mainly due to noise, though there is also a slight tendency to underestimate the magnitude of peaks.

- **Absolute difference** (continuous curves in Figure 22): This second indicator takes the absolute value of each difference, and provides a direct measure of the quality of the extrapolations. It offers a numerical assessment similar to RMSE but was preferred for comparison with the classic difference (dotted curves).

$\forall j \in [1 : 240]$, corresponding to the number of months elapsed since the start of the extrapolation, we have:

$$\text{Absolute difference} = \frac{\sum_{i=1}^{504} |\text{Extrapolated}_i - \text{Observation}_i|}{504} \quad (25)$$

Naturally, we expect this indicator to increase as j increases since we are further from the intentional end of the time series (and therefore the modeling is of lower quality)

For ONI (blue continuous curve), the values remain within an acceptable range (below 0.5) for the first 21 months, indicating generally good quality. For SOI (pink continuous curve), the values are relatively high, suggesting less accurate extrapolations.

It is important to note that these averages mask substantial differences between the simulations. Another approach is to examine the correlation between extrapolated

Difference between extrapolation and observation for ENSO indices

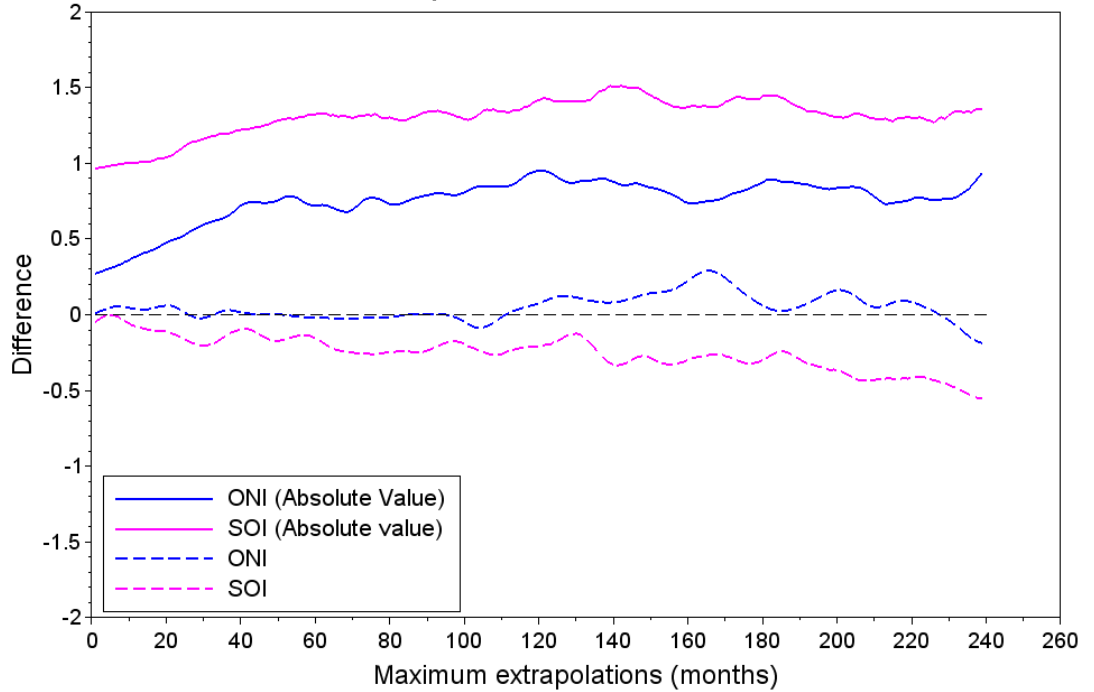


Figure 22: Difference between extrapolation and modeling for the ONI index (blue) and the SOI index (pink).

The dotted curves represent the difference (Equation 24), while the continuous curves represent the absolute difference (Equation 25). The dotted black line is located at 0, separating underestimations from overestimations.

and observed datasets (for the same months). To assess the predictive capability of the algorithm, we created datasets ranging from 2 months (the first two months extrapolated) to 20 years (240 m.) for each simulation. The average correlations from the 504 simulations are presented in Figure 23.

Correlation between extrapolation and observation for ENSO indices

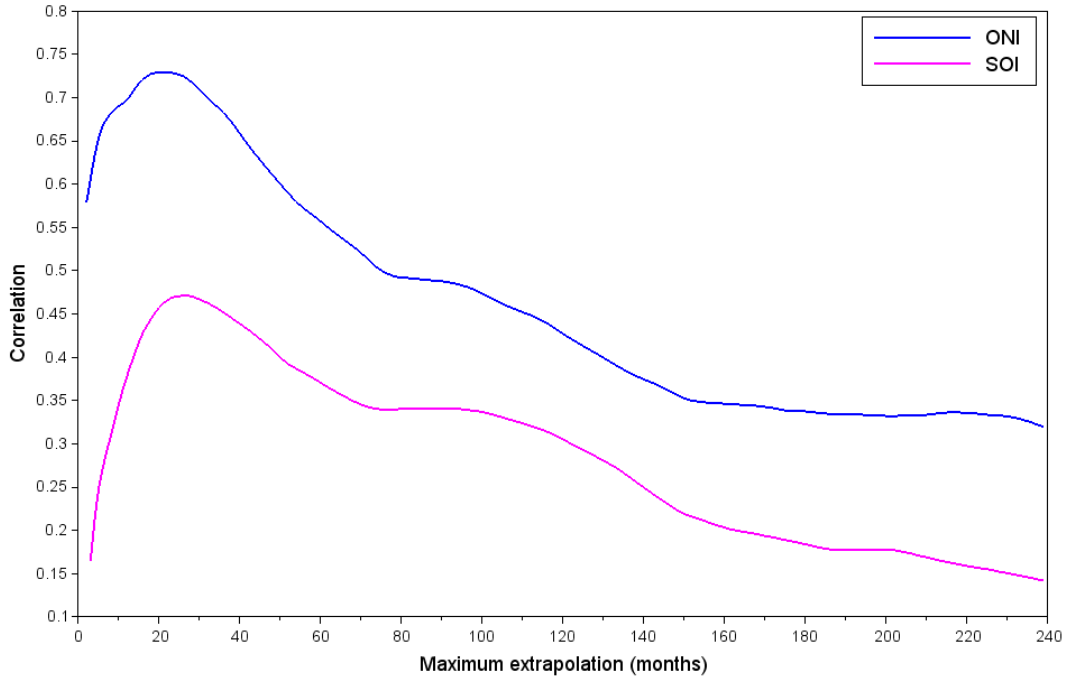


Figure 23: Correlation between extrapolation and modeling for the ONI index (blue) and the SOI index (pink).

Initial correlations show lower values. However, this does not indicate poor modeling but rather a lack of data for calculating the correlation. Between 13 months and 32 months, the correlation exceeds 0.7 for ONI, which corresponds to good quality. After 3 years (36 m.), the correlation is still equal to 0.68. In contrast, for SOI, the correlation never reaches 0.5, which is rather poor.

To address the initial issue of low correlations, we implemented an alternative method for calculating these values. Instead of looking at correlations simulation by simulation, we generated a continuous "extrapolated" signal (from different simulations) that contains the extrapolated index values for every time point. This approach allowed me to calculate the correlation between this entire extrapolated signal and the actual observed signal, leading to much higher correlation values.

This operation was repeated for all the distance to the (artificial) end of the time series, from 1 month to 20 years (240 m.). The results are illustrated in Figure 24.

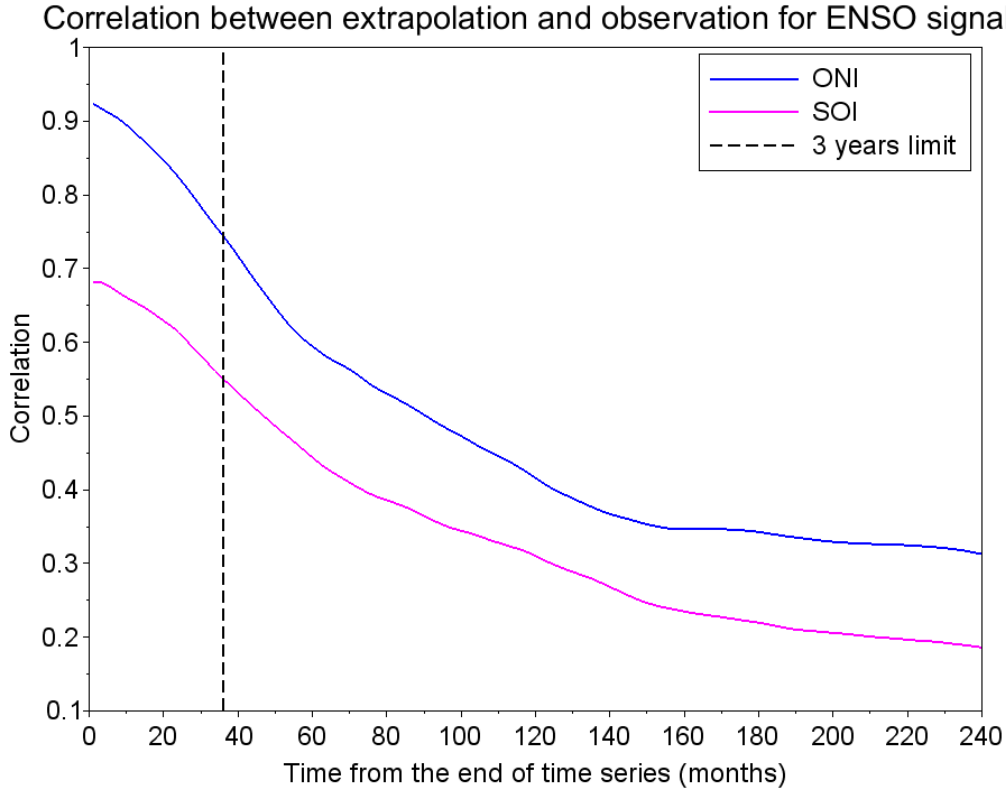


Figure 24: Correlation between extrapolation and modeling for the ONI index (blue) and the SOI index (pink).

The black dotted line corresponds to 3 years (36 m.)

As seen, the initial correlations are significantly higher. For the ONI index, the first correlation is equal to 0.92, which is very close to the reconstruction correlation of 0.94 (See Section 5.3). However, the correlation gradually decreases as time progresses, falling below 0.75 after three years. In contrast, the SOI index shows notably lower correlation values throughout the extrapolation period, with a correlation value of 0.68 after 1 month and 0.55 after 3 years.

Finally, to conclude this subsection, the quality of the extrapolations over time was examined. Linear regressions and correlations were performed, and these indicators were observed as a function of time. However, no significant trends were found.

6.3 Future predictions

As discussed, the ONI predictions appear to be reliable for 2-3 years. The most recent available data for 2024 (up to May 2024) were then added to the initial observation signal to re-run the model and perform an extrapolation (NOAA nodate) which is shown in Figure 25.

From May 2023 to April 2024, the ONI data indicated an El Niño situation, which returned to an ENSO-neutral state in May 2024. The extrapolation data first show a resurgence of the El Niño phenomenon until January 2025, a pattern previously observed several times in past data (e.g., in 1970). Then, the situation transitions to a Multiyear La Niña from April 2025 to December 2026.

The SOI index was not extrapolated due to its poor quality.

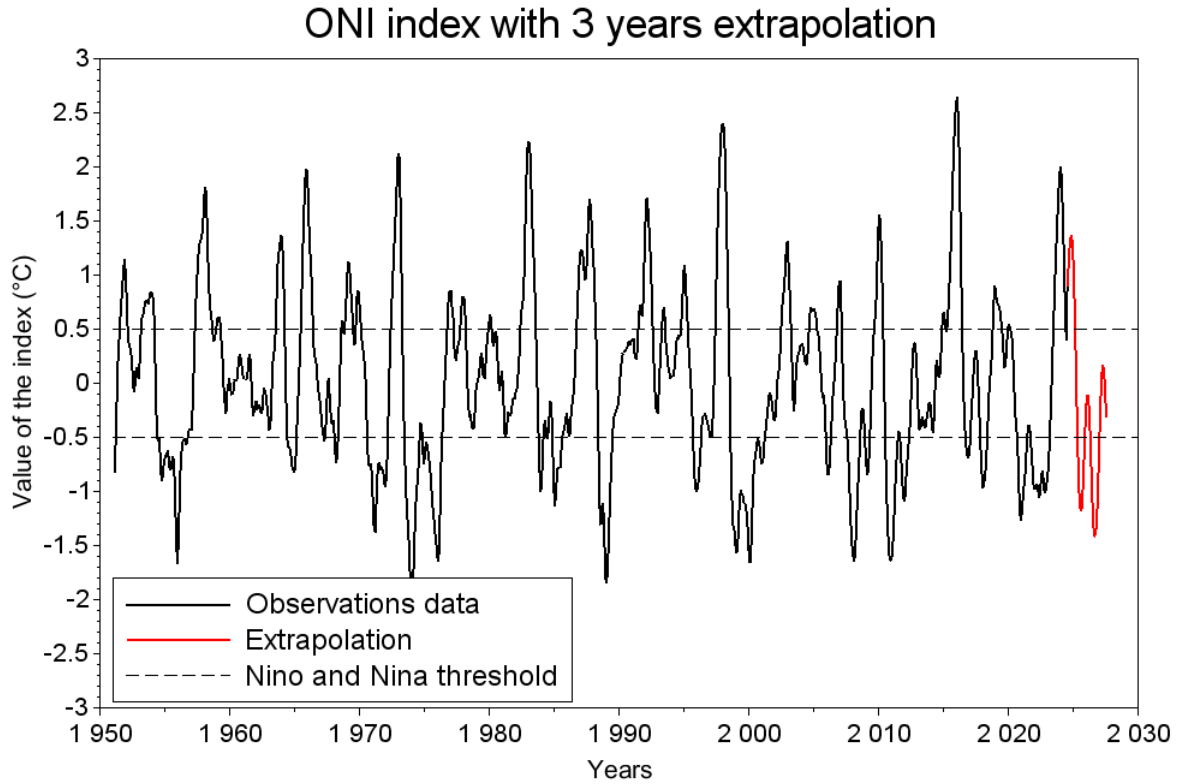


Figure 25: Observation (black curve) and 3 years extrapolation (red curve) for ONI index. The black dotted lines represent the ONI criterium for Niño and Niña events. Amplitude was extrapolated while phase and period were considered constant

7 Seventh part: Discussion

To conclude this work, we will move on to a crucial step in any scientific research: the discussion. It is divided into two main elements.

First, the correspondence between the expected and obtained results. In this subsection, we will critically address the results of temperature and ENSO. To assist this, we will connect the results obtained by WIME with the existing literature, whether related to wavelets (and more precisely Morlet-like wavelets) or not. We will then synthesise the evolution (in time and frequency) of the different components and see how this could be related to climate change.

The second element to be discussed covers the limitations and perspectives of the work done. We will present the usefulness of predicting this index, a new and more precise extrapolation method, and new indices and phenomena to which the method could be applied.

7.1 Correspondence between expected and obtained results

7.1.1 Cycles in Temperature

As we saw in Section 4, the new version of WIME detected various expected cycles. Indeed, the 1-year cycle (orbit around the sun), the 6-month cycle (ephemeris), the 30-month cycle (AO-NAO), and the 22-year cycle (sun) all have physical explanations.

Regarding the solar activity cycle, some cycles described in Mabillet's PhD (2014)⁵ were detected by WIME, although they are much less energetic (and thus not mentioned in Section 4). Indeed, WIME detects the 18.2-month cycle⁶ and the 39 month cycle⁷, both linked to solar activity, although it should be noted that they vary temporally.

Regarding the 43-month cycle studied by Pr. Georges Mabillet, it was expected that we would not observe it since it is induced by the ENSO phenomenon, whose teleconnections in Europe are too weak to reveal this cycle at Bierset (Mabillet **and others** 2012),.

Thus, we can say that the main cycles expected in the temperatures of Bierset were all detected by WIME, confirming the robustness of the algorithm and its improvement in this thesis. Consequently, we can hypothesise that it will also work on ENSO indices.

7.1.2 Cycles in ENSO indices

The first factor that enhances confidence in the results is the observation that both ONI and SOI indices, when analysed, show similar periods.

In addition, we have to consider the scientific literature, noting that it is more complicated to determine the expected results for ENSO cycles due to the lesser consensus in the literature compared to temperature cycles.

In Table 8, we compare the cycles detected by WIME (in both ONI and SOI signals) with those identified in Mabillet's PhD (2014) and with findings from a broader range of scientific literature (Bruun **and others** 2017; Y. Li 2024; Ren **and** R. Wang 2023;

⁵Thesis conducted using a Morlet-wavelet analysis

⁶period 8: 17.9 months

⁷period 11: 37.0 months

B. D. Dommenget **and** Al-Ansari 2023; Jajcay **and others** 2018).

WIME	Mabille PhD	General litterature
12.5 years (low)	-	12 years
4.0-6.50 years (mid)	5 years (60 m.)	4.3, 4.6, 4-5, 5, 5-6 years
2.5 years (high)	2.5 years (30 m.)	2.3, 2.5, 2.5 years
1.4 years (high)	-	1.7, 1.8 years

Table 8: Periods in ENSO indices

We can see that the four major cycles identified by WIME have all been described in the literature. Low-frequency periods appear to be the least documented. The 12-year cycle was mentioned by Bruun **and others** (2017), which hypothesizes a link with the solar cycle and suggests that this could lead to prolonged periods favorable to either El Niño or La Niña conditions.

Regarding mid-frequencies, the literature reports various cycles ranging from 4 to 6 years in all the cited scientific articles. However, we should note the 42-month cycle (3.5 years), detected in wavelet analyses as well as in the literature (B. D. Dommenget **and** Al-Ansari 2023; Bruun **and others** 2017), does not appear in WIME’s results.

The 2.5-year mode is detected in nearly all the mentioned literature and is believed to have a major influence on ENSO. This period is associated with the quasi-biennial oscillation, which corresponds to changes in wind direction and creates an alternation between ”strong” and ”weak” years in the Indian Ocean and the Pacific (Jajcay **and others** 2018; Bruun **and others** 2017).

The 1.4-year cycle, on the other hand, could potentially be associated with the 1.7-1.8 year cycle (B. D. Dommenget **and** Al-Ansari 2023). This is the highest frequency detected by WIME, as it corresponds to the timescale of a single ENSO event.

Both high-frequency periods would be influenced by mid-frequency periods, affecting both their frequency and amplitude (Jajcay **and others** 2018).

7.1.3 Potential impact of Global Change

According to several recent studies (Z. Chen **and others** 2024; Jiang **and** Zhu 2018; Xia **and others** 2017), climate change is expected to increase the frequency, intensity

and lifespan of ENSO events. Thus, we can anticipate an increase in amplitude and a decrease in period (therefore, an increase in frequency). These changes should be observable in both past periods and future extrapolations.

The majority of amplitudes and periods have fluctuated. Therefore, while it is interesting to consider recent increases or decreases for extrapolations, these do not necessarily indicate a long-term change potentially induced by climate change.

In Table 9, the behavior of amplitude and frequency for both the ONI and SOI indices over the past decades is summarized. The mention "Osc." indicates an increase or decrease of less than 10 years (and reflects frequent fluctuations throughout the time series). From the 7 periods present (per index), we observe the following:

- **ONI Amplitudes:** 4 increases and 1 decrease
- **SOI Amplitudes:** 2 increases (corresponding to two of the three most influential periods) and 2 decreases
- **ONI Frequencies:** 1 increase and 2 decreases
- **SOI Frequencies:** 1 increase and 2 decreases

Periods	Amplitude		Frequency	
	ONI	SOI	ONI	SOI
A. 12.5 years (low)	Osc.	+	Osc.	-
B. 9 years (low)	+	////////////////	-	////////
C. 4.0-6.50 years (mid)	+ and - and Stable	Stable and - +	Osc. and Osc. Stable	- and Osc. +
D. 2.5 years (high)	+	Osc.	-	Osc.
E. 1.4 years (high)	+	-	+	Osc.
F. 1 years (high)	////////	Osc.	////////	Osc.

Table 9: Evolution (past and future) of the amplitude and frequency of different periods (detected by WIME) in ENSO indices

"+" indicates an increase and "-" indicates a decrease

"Osc." means that the change ("+" or "-") is too recent to draw conclusions

There would thus be a dominant trend towards an increase in the amplitude and a decrease in the frequency of ENSO events. This conclusion does not quite align with the scientific literature, which forecasts an increase in frequency in addition to an increase in amplitude (Z. Chen **and others** 2024; Xia **and others** 2017).

7.2 Limitations and perspectives

In this second subsection of the discussion, we address some of the choices made in achieving the work relating to this Master thesis and examine to what extent they represent limitations, which could also serve as potential avenues for future research.

7.2.1 A usefulness for predictions

The primary objective of predicting the ENSO phenomenon is to provide society and its authorities with useful information for the mitigation of climate-related risks. Each phase of the ENSO cycle is associated with consequences depending on the region. Accurate predictions (both short-term and mediumterm) could therefore enable society to adapt to and prepare for the impacts of these events, thereby reducing negative humanitarian, societal, and economic consequences.

For example, protective measures could involve assuring help to (or even evacuating) populated areas, choosing crops and agricultural practices suited to the ENSO phase, developing supply policies, and implementing measures to protect biodiversity, etc.

A concrete and very recent example of an utility of predicting future ENSO events, by proactive adaptation is detailed by Mugiyo **and others** (2023). In Zimbabwe, El Niño events have causes significant drought and lead to a considerable reduction in maize yields. To mitigate the effect of the El Niño event in 2023-2024, the Zimbabwean government has recommended several strategies for farmers, such as planting drought-resistant crop varieties and selecting livestock species that are more resilient to heat and water scarcity.

Furthermore, it would be valuable to investigate whether Earth System Models (ESMs), such as those used in IPCC reports, can simulate these fluctuation periods without the assimilation of observational data. If these fluctuations are reproduced by ESMs, it would indicate that the periods in question are driven by the few forcing factors included in these models, such as solar activity, aerosols, and greenhouse gas concentrations. Conversely, if these periods are not well represented in the ESMs, it would suggest that these models may need adjustments. Identifying these cycles could then help improve the accuracy of current climate models by incorporating the ENSO phenomenon more effectively.

7.2.2 Periods and phase extrapolations

We have observed that the various cosine components vary in amplitude, frequency, and phase. However, in the predictions section (Section 6), only the amplitude was extrapolated, while the period and phase were assumed to be constant. This represents a first limitation of the work reported in this thesis.

To allow for the extrapolation of the period, we can refer back to Equation 16.

$$c_i(t) = 2|A_i^*(t)| \cos[\arg W_i^*(t)]$$

As mentioned in Section 3.3.2, the term $\arg W_i^*$ encompasses both frequency and phase, which evolve over time, as follows:

$$\arg W_i^* = 2\pi \frac{1}{\xi_i^*(t)} + \phi_i^*(t)$$

With ϕ_i^* representing the phase and $\xi_i^*(t)$ the period.

Thus, to further improve the quality of the extrapolation of the component c_i , an extrapolation of the period $\xi_i^*(t)$ was performed. This method is very similar to the extrapolation of amplitude (Section 6.1.1), except that since the ridge function is a **step function**, it was necessary to first perform a spline interpolation to obtain a curve and allow for the detection of IPs. An example is presented on Figure 26.

The correlation and absolute difference values were assessed using the same 504 simulations as those conducted during the validation of the prediction without period extrapolation (Section 6.2). It appears that this decreases the quality of the predictions.

The results of this new extrapolation are still presented for ONI in Figure 27. It can be observed that the results are similar to those described in the initial prediction (Section 6). The extrapolation starts with a slight resurgence of the warm phase (El Niño) and then transitions to the cold phase (La Niña). The La Niña phase would begin slightly later (August 2025) and continue until February 2027. Instead of a multi-year La Niña as previously described, we would see a long, pronounced peak.

Thus, to further enhance the quality of the extrapolation, one might also consider extrapolating the phase ϕ_i^* .

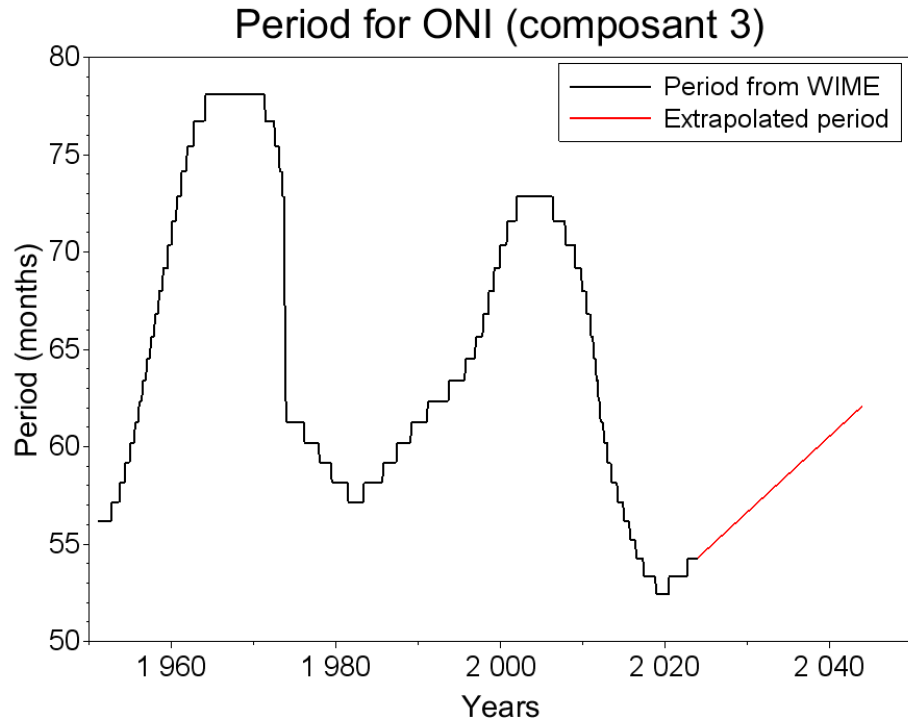


Figure 26: Evolution of the amplitude for 3rd ONI component c_3 (black), with 20 years extrapolation (red).

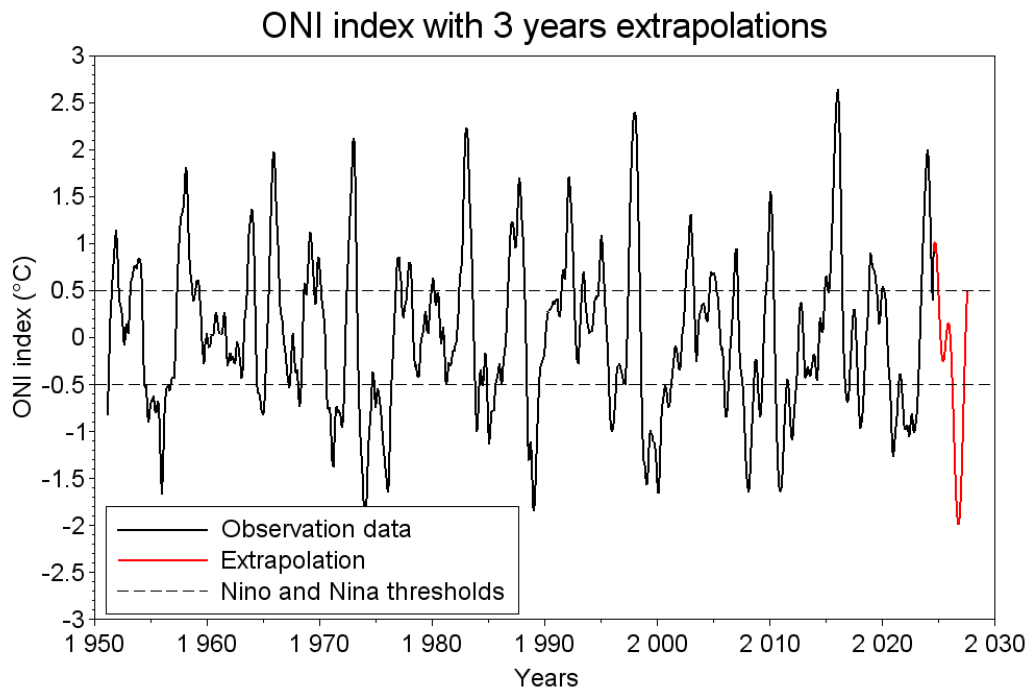


Figure 27: Observation (black curve) and 3 years extrapolation (red curve) for ONI index. The black dotted lines represent the ONI criterium for Niño and Niña events. Amplitude and ridge were extrapolated while phase was considered constant.

7.2.3 ENSO indices chosen

As previously explained, the ENSO phenomenon influences the entire dynamics of the Pacific (and beyond), where various climate variables can be used to describe this phenomenon.

The most commonly used variable is the Pacific Ocean temperature. By measuring it in four "Niño regions" (as shown in Figure 11), different aspects of the ENSO phenomenon can be highlighted:

- **Niño 1.2:** These two regions, almost always combined, are located off the coast of Latin America. They reflect directly the upwelling (or the absence of upwelling) of cold water, which can sometimes allow for earlier detection of an El Niño (Wei 2024).
- **Niño 3 and Niño 4:** These two regions are highly correlated, but the difference between these two indices helps differentiate canonical El Niño events from Modoki events (Ren and Jin 2011).
- **Niño 3.4:** This is the most commonly used region and is the one measured to calculate the ONI index used in this thesis (NOAA 2024b). The water temperature in this region is considered the strongest index to represent the global influence of ENSO (X. Li and others 2023).

Additionally, variables include surface atmospheric pressure (the SOI index used in this thesis), as well as Outgoing Longwave Radiation (OLR), which is higher during El Niño phases. Winds, sea level, precipitation, and various combinations of these variables can also serve as indicators. NOAA provides 15 different indices, and other indices created by different authors can be added to this list (NOAA 2024a; X. Li and others 2023).

This broad range of indices helps to understand the complex ENSO phenomenon in its entirety. Although correlated, these indices can be quite different from each other. This was evident when noting the correlation of only 0.73 between ONI and the reversed SOI ⁸. The SOI is much noisier than ONI (NOAA 2024a).

Therefore, studying only two of these indices is a second limitation of the work reported here, even though we focused on the two indices often considered to be the most representative and with a complete time series since 1951. Moreover,

⁸As previously mentioned, SOI is naturally anti-correlated with ONI (Section 5.1)

choosing ONI and SOI appears to be logical because they help to understand the two main sides of the ENSO phenomenon respectively oceanic and atmospheric components. However, WIME should be applied to other variables and Niño regions as a perspective.

7.2.4 Perspectives for other phenomena

The final perspective of this discussion concerns the mathematical methodology used rather than the ENSO phenomenon itself. Indeed, we have seen that the wavelet approach, and even the code of the new version of WIME, has successfully revealed cycles and predicted a complex signal such as ENSO. This methodology could therefore be applied to other complex phenomena, such as the quasi-biennial oscillation (QBO), the AO, the NAO, as well as geological signals such as the Milankovitch cycles or the Earth's magnetic field.

To extrapolate further, it is possible that some phenomena that appear random might also be governed by natural cycles and could potentially be predicted using a methodology like WIME. For instance, earthquakes might follow cycles on the order of hundreds or even thousands of years (Demoulin 2008).

8 Conclusions

ENSO is a complex phenomenon that seems to occur with irregular periodicity. In this thesis, we sought to improve the understanding of the cycles that govern it, as well as their evolution in frequency and amplitude. These results, already interesting in themselves, could enable future subsequent predictions (over 3 years). We propose the application of a medium-term prediction method.

To achieve the results anticipated, we employed a modal extraction method based on Continuous Wavelet Transforms (CWT). Besides demonstrating its effectiveness on temperature measurements, the efficacy of this method on ENSO was proven in this thesis through:

- **The quality of ONI reconstruction:** a correlation of 0.94 and an RMSE of 0.39°C for the ONI index; and an efficiency of 90% for binary detection of El Niño and La Niña events.
- **The correspondence of detected periods:** The agreement of periods between the two studied indices (ONI and SOI), as well as with the literature, demonstrates the real existence of the cycles detected in this thesis.
- **The quality of ONI extrapolation:** an average correlation that can reach 0.7 after more than a year, and a difference between modeling and observations of less than 0.5°C for the first 21 months.

Given the importance of the phenomenon in climate dynamics, this advancement opens various perspectives, such as improving climate prediction models.

References

- Alladi, Hemanth Kumar, P.R. Satheesh Chandran **and** Venkat Ratnam M (2024). “Impact of ENSO on the UTLS chemical composition in the Asian Summer Monsoon Anticyclone”. *in Atmospheric Research*: 309. DOI: 10.1016/j.atmosres.2024.107551.
- Arcodia, Marybeth C., Emily Becker **and** Ben P. Kirtman (2024). “Subseasonal Variability of U.S. Coastal Sea Level from MJO and ENSO Teleconnection Interference”. *in Weather and Forecasting*: 39.2, **pages** 441–458. DOI: 10.1175/WAF-D-23-0002.1.
- Ashok, K. **and** T. Yamagata (2009). “The El Niño with a difference.” *in Nature*: 461.481-484. DOI: <https://doi.org/10.1038/461481a>.
- Avalon-Cullen, Cheila, Rafea Al Suhili, Nathaniel K. Newlands, Christy Caudill, Harvey Hill, Jaqueline Spence-Hemmings **and** Markus Enenkel (2024). “ENSO Impacts on Jamaican Rainfall Patterns: Insights from CHIRPS High-Resolution Data for Disaster Risk Management”. *in GeoHazards*: 5.1, **pages** 91–111. DOI: 10.3390/geohazards5010005.
- Beverley, J.D., M. Collins, F.H. Lambert **and** R. Chadwick (2024). “Drivers of Changes to the ENSO–Europe Teleconnection Under Future Warming”. *in Geophysical Research Letters*: 51.10. DOI: 10.1029/2023GL107957.
- Bruun, T., I. Allen **and** T. Smyth (2017). “Heartbeat of the Southern Oscillation explains ENSO climatic resonances”. *in JGR Oceans*: 122, **pages** 6746–6772. DOI: 10.1002/2017JC012892.
- Chen, M. **and** T. Li (2018). “Why 1986 El Niño and 2005 La Niña evolved different from a typical El Niño and La Niña”. *in Clim Dyn*: 51, **pages** 4309–4327. DOI: 10.1007/s00382-017-3852-1. URL: <https://doi.org/10.1007/s00382-017-3852-1>.
- Chen, Zhiping, Li Li, Bingkun Wang, Jiao Fan, Tieding Lu **and** Kaiyun Lv (2024). “The impact of global warming on ENSO from the perspective of objective signals”. *in Atmospheric Research*: 299, **page** 107176. ISSN: 0169-8095. DOI: <https://doi.org/10.1016/j.atmosres.2023.107176>.
- Cordero, Raúl R., Sarah Feron, Alessandro Damiani, Jorge Carrasco, Cyrus Karas, Chenghao Wang, Clarisse T. Kraamwinkel **and** Anne Beaulieu (2024). “Extreme fire weather in Chile driven by climate change and El Niño–Southern Oscillation (ENSO)”. *in Scientific Reports*: 14.1. DOI: 10.1038/s41598-024-52481-x.
- Deivanayagam, Aarthi, Ranjit Kumar Sarangi **and** Masilamani Palanisamy (2024). “Evaluating the Influence of El Nino–Southern Oscillation (ENSO) Patterns on the Spatio-Temporal Variations of Drought over Southern Peninsular Indian

- Region”. **in** *Journal of the Indian Society of Remote Sensing*: 52.3, **pages** 463–484. DOI: 10.1007/s12524-022-01589-6.
- Deliège, A. **and** S. Nicolay (2017). “Extracting oscillating components from nonstationary time series: A wavelet-induced method”. **in** *Phys. Rev. E*: 96 (3), **page** 033307. DOI: 10.1103/PhysRevE.96.033307. URL: <https://link.aps.org/doi/10.1103/PhysRevE.96.033307>.
- Demoulin, A. (2008). *Risques naturels: Tremblements de terre*. unpublished.
- Deng, Wenjie, Jing Zhang, Siteng Justin Zhu, Keiji Horikawa, Takahiro Endoh, Takeshi Matsuno, Yoshiko Kondo, Mutsuo Inoue **and** Seiya Nagao (**july** 2024). “Origins of Low-Oxygen Bottom Water Influenced by Tide and ENSO on the Outer-Edge Shelf of East China Sea: Multi-Chemical Tracer Approaches”. **in** *Journal of Geophysical Research: Oceans*: 129.7. ISSN: 2169-9275. DOI: 10.1029/2024JC020917.
- Dogar, Muhammad Mubashar, Fred Kucharski, Tomonori Sato, Shahbaz Mehmood, Shaukat Ali, Zhiqiang Gong, Debanjana Das **and** Josefina Arraut (2019). “Towards understanding the global and regional climatic impacts of Modoki magnitude”. **in** *Global and Planetary Change*: 172, **pages** 223–241. ISSN: 0921-8181. DOI: <https://doi.org/10.1016/j.gloplacha.2018.10.004>.
- Dommenget, B. D. **and** M. Al-Ansari (2023). “Asymmetries in the ENSO phase space”. **in** *Climate Dynamics*: 60, **pages** 2147–2166. DOI: 10.1007/s00382-022-06392-0. URL: <https://doi.org/10.1007/s00382-022-06392-0>.
- Dommenget, D., T. Bayr **and** C. Frauen (2013). “Analysis of the non-linearity in the pattern and time evolution of El Niño southern oscillation”. **in** *Clim Dyn*: 40, **pages** 2825–2847. DOI: 10.1007/s00382-012-1475-0.
- Eggeling, Jakob, Chuansi Gao, Dong An, Raul Cruz-Cano, Hao He, Linus Zhang, Yu-Chun Wang **and** Amir Sapkota (2024). “Spatiotemporal link between El Niño Southern Oscillation (ENSO), extreme heat, and thermal stress in the Asia–Pacific region”. **in** *Scientific Reports*: 14.1. DOI: 10.1038/s41598-024-58288-0.
- Espinoza, Vicente, Felipe Lobos-Roco **and** Camilo del Río (2024). “Synoptic control of the spatiotemporal variability of fog and low clouds under ENSO phenomena along the Chilean coast (17°–36° S)”. **in** *Atmospheric Research*: 308. DOI: 10.1016/j.atmosres.2024.107533.
- Eusebi Borzelli, G.L. **and** S. Carniel (2023). “Where the winds clash: what is really triggering El Niño initiation?” **in** *npj Clim Atmos Sci*: 6, **page** 119. DOI: 10.1038/s41612-023-00445-9. URL: <https://doi.org/10.1038/s41612-023-00445-9>.
- Frigio, Matteo **and** Steven G. Johnson (2005). “The Design and Implementation of FFTW3”. **in** *Proc. IEEE*: 93 (2), **pages** 216–231.

- Gregory, Catherine H., Neil J. Holbrook, Claire M. Spillman **and** Andrew G. Marshall (2024). “Combined Role of the MJO and ENSO in Shaping Extreme Warming Patterns and Coral Bleaching Risk in the Great Barrier Reef”. *in Geophysical Research Letters*: 51.13. DOI: 10.1029/2024GL108810. URL: <https://www.scopus.com/inward/record.uri?eid=2-s2.0-85197274708&doi=10.1029/2f2024GL108810&partnerID=40&md5=d2c9a770e39215b94ef8c02569d62cbf>.
- Gurdjian, Chloé (2023). *Les effets catastrophiques du phénomène El Niño sur les animaux*. <https://www.geo.fr/animaux/les-effets-catastrophiques-du-phenomene-el-nino-sur-les-animaux-secheresse-eau-inondations-nourriture-217503>. website. accessed 05 march 2024.
- He, L., X. Hao **and** T. Han (2021). “The asymmetric impacts of ENSO modoki on boreal winter climate over the Pacific and its rim”. *in Clim Dyn*: 56, **pages** 29–44. DOI: 10.1007/s00382-020-05395-z.
- Hsiang, Solomon M., Kyle C. Meng **and** Mark A. Cane (2011). “Civil conflicts are associated with the global climate”. *in Nature*: 476.7361, **pages** 438–441. DOI: 10.1038/nature10311. URL: <https://doi.org/10.1038/nature10311>.
- Huang, Ping, Yue Chen, Jinbao Li **and** Hong Yan (2024). “Redefined background state in the tropical Pacific resolves the entanglement between the background state and ENSO”. *in npj Climate and Atmospheric Science*: 7, **page** 147. DOI: 10.1038/s41612-024-00695-1.
- IPPC (2023). *Climate Change 2023: Synthesis Report. Contribution of Working Groups I, II and III to the Sixth Assessment Report of the Intergovernmental Panel on Climate Change Core Writing Team, H. Lee and J. Romero (eds.)* Geneva, Switzerland: IPCC, **page** 184. DOI: 10.59327/IPCC/AR6-9789291691647.
- Jadhav, J., S. Panickal, S. Marathe **and** et al. (2015). “On the possible cause of distinct El Niño types in the recent decades”. *in Sci Rep*: 5, **page** 17009. DOI: 10.1038/srep17009.
- Jajcay, N., S. Kravtsov, G. Sugihara, Tsonis; A. **and** M. Paluš (2018). “Synchronization and causality across time scales in El Niño Southern Oscillation”. *in npj Climate and Atmospheric Science*: 1, **page** 33. DOI: 10.1038/s41612-018-0043-7.
- Jiang, Ning **and** Congwen Zhu (2018). “Asymmetric Changes of ENSO Diversity Modulated by the Cold Tongue Mode Under Recent Global Warming”. *in Geophysical Research Letters*: 45.22, **pages** 12, 506–12, 513. DOI: 10.1029/2018GL079494.
- Jin-Yi Yu, Hsun-Ying Kao **and** Tong Lee (2010). “Subtropics-Related Interannual Sea Surface Temperature Variability in the Central Equatorial Pacific”. *in Journal of Climate*: 23, **pages** 2869–2884. DOI: <https://doi.org/10.1175/2010JCLI3171.1>.

- Kulkarni, M. N. **and** D. Siingh (2016). “The atmospheric electrical index for ENSO modoki: Is ENSO modoki one of the factors responsible for the warming trend slowdown?” *in Sci. Rep.*: 6, **page** 24009. DOI: 10.1038/srep24009.
- Li, Xiaofan, Zeng-Zhen Hu, Ruiqiang Ding **and** Yunyun Liu (2023). “Which ENSO index best represents its global influences?” *in Climate Dynamics*: 61.9-10, **pages** 4899–4913. DOI: 10.1007/s00382-023-06804-9. URL: <https://www.scopus.com/inward/record.uri?eid=2-s2.0-85160414667&doi=10.1007%2fs00382-023-06804-9&partnerID=40&md5=4e2b7b73f93531d117fb17a565b9d9e6>.
- Li, Yaokun (2024). “A spatiotemporal oscillator model for ENSO”. *in Theoretical and Applied Climatology*: 155.4, **pages** 3281–3296. ISSN: 1434-4483. DOI: 10.1007/s00704-023-04809-2.
- Mabille, Georges (2014). “Analyse de la variabilité naturelle du climat : application à l’aide des ondelettes”. phdthesis. Université de Liège.
- Mabille, Georges, Xavier Fettweis, Michel Erpicum **and** Samuel Nicolay (2012). “Étude fréquentielle de données via la transformée en ondelette : application aux cycles climatiques”. *in BSGLe*: 58, **pages** 5–15.
- Mueller, Teryn J., Christina M. Patricola **and** Emily Bercos-Hickey (2024). “The Influence of ENSO Diversity on Future Atlantic Tropical Cyclone Activity”. *in Journal of Climate*: 37.15, **pages** 3959–3975. DOI: 10.1175/JCLI-D-23-0286.1.
- Nájera González, Oyolsi, Areli Nájera González, Susana M. L. Marceléno Flores **and** Fernando Flores Vilchez (2024). “Influence of ENSO and the urban heat island on climate variation in a growing city of the western Mexico”. *in One Ecosystem*: 9. DOI: 10.3897/oneeco.9.e125302.
- NASA, Goddard Space Flight Center (2011). *The Solar Cycle*. https://svs.gsfc.nasa.gov/10804/#section_credits. accessed 30 july 2024.
- Nicolay, Samuel (2006). “Analyse de séquences ADN par la transformée en ondelettes : extraction d’informations structurelles, dynamiques et fonctionnelles”. phdthesis. Université de Liège.
- NOAA (2024a). *El Niño-Southern Oscillation (ENSO) Dashboard*. Accessed: 2024-08-01. URL: <https://psl.noaa.gov/enso/dashboard.html>.
- (2024b). *Equatorial Pacific Sea Surface Temperature SST. Climate monitoring - ENSO*. <https://www.ncei.noaa.gov/access/monitoring/enso/sst>. website. accessed 15 February 2024. National Oceanic Atmospheric Administration.
- (2024c). *Southern Oscillation Index SOI. Climate monitoring - ENSO*. <https://www.ncei.noaa.gov/access/monitoring/enso/soi>. website. accessed 15 February 2024. National Oceanic Atmospheric Administration.

- NOAA (nodate). *Climate Prediction Center. Monitoring and data- Oceanic and atmospheric data - Monthly atmospheric and SST indice - Equatorial SOI and Sea surface temperature SST*. <https://www.cpc.ncep.noaa.gov/data/indices/>. website. accessed 10 February 2024. National Oceanic Atmospheric Administration NOAA.
- Nurdiati, Sri, Fahren Bukhari, Ardhasena Sopaheluwakan, Pandu Septiawan **and** Vicho Hutapea (2024). “ENSO AND IOD IMPACT ANALYSIS OF EXTREME CLIMATE CONDITION IN PAPUA, INDONESIA”. *in Geographia Technica*: 19.1, **pages** 1–18. DOI: 10.21163/GT_2024.191.01.
- Oppenheim, Alan V. **and** Ronald W. Schaffer (1975). *Digital Signal Processing*. Englewood Cliffs, NJ: Prentice Hall. ISBN: 9780132146357.
- Pal, M., R. Maity, J.V. Ratnam **and** et al. (2020). “Long-lead Prediction of ENSO Modoki Index using Machine Learning algorithms”. *in Sci Rep*: 10, **page** 365. DOI: 10.1038/s41598-019-57183-3. URL: <https://doi.org/10.1038/s41598-019-57183-3>.
- Pelckmans, Ignace, Jean-Philippe Belliard, Olivier Gourgue, Luis Elvin Dominguez-Granda **and** Stijn Temmerman (2024). “Mangroves as nature-based mitigation for ENSO-driven compound flood risks in a large river delta”. *in Hydrology and Earth System Sciences*: 28.6, **pages** 1463–1476. DOI: 10.5194/hess-28-1463-2024.
- Ren, Hong-Li **and** Fei-Fei Jin (2011). “Niño indices for two types of ENSO”. *in Geophysical Research Letters*: 38.4. DOI: <https://doi.org/10.1029/2010GL046031>.
- Ren, Hong-Li **and** Run Wang (2023). “Diagnosing the Linear Periodicity Dynamics of ENSO for Its Two Spatiotemporal Modes”. *in Geophysical Research Letters*: 50, e2023GL105756. DOI: 10.1029/2023GL105756.
- Rodrigues, Julia Isabella de Matos, Walmer Bruno Rocha Martins, Victor Pereira de Oliveira, Myriam Suelen da Silva Wanzerley, Hélio Brito dos Santos Júnior **and** Francisco de Assis Oliveira (2024). “ENSO impacts on litter stocks and water holding capacity in secondary forests in eastern Amazonia”. *in Journal of Forestry Research*: 35.1. DOI: 10.1007/s11676-023-01665-8. URL: <https://www.scopus.com/inward/record.uri?eid=2-s2.0-85178930518&doi=10.1007%2fs11676-023-01665-8&partnerID=40&md5=d22273f2f8bef1ed292e279f1e8a90b3>.
- Saint-Lu, Marion **and** Julie Leloup (2016). “Petit précis de théorie pour comprendre El Niño”. *in La Météorologie*: 95.8, **pages** 30–38. DOI: 10.4267/2042/61615. URL: <https://hal.archives-ouvertes.fr/hal-01491804>.
- Shikwambana, Lerato, Mahlatse Kganyago **and** Sifiso Xulu (2022). “Analysis of wildfires and associated emissions during the recent strong ENSO phases in Southern Africa using multi-source remotely-derived products”. *in Geocarto International*: 37.27, **pages** 16654–16670. DOI: 10.1080/10106049.2022.2113449.

- Shukla, Shraddhanand, Fahim Zaheer, Andrew Hoell, Weston Anderson, Harikishan Jayanthi, Greg Husak, Donghoon Lee, Brian Barker, Shahriar Pervez, Kimberly Slinski, Christina Justice, James Rowland, Amy L. McNally, Michael Budde **and** James Verdin (2024). “ENSO-based outlook of droughts and agricultural outcomes in Afghanistan”. *in Weather and Climate Extremes*: 45. DOI: 10.1016/j.wace.2024.100697. URL: <https://www.scopus.com/inward/record.uri?eid=2-s2.0-85195577235&doi=10.1016%2fj.wace.2024.100697&partnerID=40&md5=fc245f36e3b27473983a0ece5ed1bec0>.
- Smith, S. C. **and** D. Ubilava (2017). “The El Niño Southern Oscillation and economic growth in the developing world”. *in Global Environmental Change*: 45, **pages** 151–164. DOI: 10.1016/j.gloenvcha.2017.05.007. URL: <https://doi.org/10.1016/j.gloenvcha.2017.05.007>.
- Vega, Johnny, Janet Barco **and** Cesar Hidalgo (2024). “Space-time analysis of the relationship between landslides occurrence, rainfall variability and ENSO in the Tropical Andean Mountain region in Colombia”. *in Landslides*: 21.6. Cited by: 0; All Open Access, Hybrid Gold Open Access, **pages** 1293–1314. DOI: 10.1007/s10346-024-02225-9. URL: <https://www.scopus.com/inward/record.uri?eid=2-s2.0-85185947775&doi=10.1007%2fs10346-024-02225-9&partnerID=40&md5=3a0f8dba3dc1ea91968c7a232e7bb543>.
- Wang, Jinfei, Hao Luo, Lejiang Yu, Xuewei Li, Paul R. Holland **and** Qinghua Yang (2023). “The Impacts of Combined SAM and ENSO on Seasonal Antarctic Sea Ice Changes”. *in Journal of Climate*: 36.11, **pages** 3553–3569. DOI: 10.1175/JCLI-D-22-0679.1.
- Wang, Mingjie, Chaoxia Yuan, Jingchan Liu, Yihua Wei, Jiye Wu **and** Jingjia Luo (2023). “Underestimated relationship between westerly wind bursts and ENSO in CMIP6 models”. *in Atmospheric and Oceanic Science Letters*: 16.6, **page** 100336. ISSN: 1674-2834. DOI: <https://doi.org/10.1016/j.aosl.2023.100336>.
- Wang, Xiaohong, Qingheng Lu, Shiyuan Zhong, Yike Yang, Yinchun Chen **and** Zunli Dai (2024). “Observational analysis of surface ozone variability in China from 2015 to 2020: Insights from consecutive ENSO episodes”. *in Atmospheric Pollution Research*: 15.8. DOI: 10.1016/j.apr.2024.102185.
- Wei, Liangtong (2024). “Summary of Commonly Used ENSO Indices”. *in Highlights in Science, Engineering and Technology IFMPT*: 88, **page** 687.
- Xia, Yang, Xuguang Sun, Yan Yan, Weiyang Feng, Fang Huang **and** Xiuqun Yang (2017). “Change of ENSO characteristics in response to global warming”. *in Kexue Tongbao/Chinese Science Bulletin*: 62.16, **pages** 1738–1751. DOI: 10.1360/N972016-01225.

- Yin, Hao, Hayley J. Fowler, Stephen Blenkinsop, Zhiyong Wu, Hai He **and** Yuan Li (2023). “ENSO and IOD contributions to seasonal meteorological droughts over the Yangtze River basin”. **in***International Journal of Climatology*: 43.16, **pages** 8120–8136. DOI: 10.1002/joc.8311.
- Yu, Jin-Yi **and** Seon Tae Kim (2011). “Relationships between Extratropical Sea Level Pressure Variations and the Central Pacific and Eastern Pacific Types of ENSO”. **in***Journal of Climate*: 24, **pages** 708–720. DOI: <https://doi.org/10.1175/2010JCLI3688.1>.
- Yu, N., H. Liu, G. Chen, W. Chen, J. Ray, H. Wen **and** N. Chao (2021). “Analysis of Relationships Between ENSO Events and Atmospheric Angular Momentum Variations”. **in***Earth and Space Science*: 8.12. DOI: <http://doi.org/10.1029/2021EA002030>.
- Zheng, Li, Qiu Lanlan, Wang Wei, He Bin, Wu Shaohong **and** He Shanfeng (2024). “Spacio-Temporal Variation Characteristics of Northward-Moving Typhoon and Their Relationship with ENSO; [ENSO]”. **in***Tropical Geography*: 44.6, **pages** 973–986. DOI: 10.13284/j.cnki.rddl.20230936.
- Zhou, Shuntai, Alvin J. Miller, Julian Wang **and** James K. Angell (2001). “Trends of NAO and AO and their associations with stratospheric processes”. **in***Geophysical Research Letters*: 28.21, **pages** 4107–4110. DOI: 10.1029/2001GL013660.